Aalto University
School of Science

Bachelor's Programme in Science and Technology

Characterizing Superconducting Resonators in an Autonomous Quantum Heat Engine

Ahmad Darwish

Bachelor's Thesis
2025

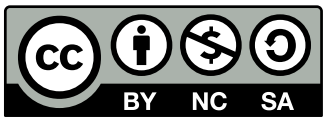

Aalto University
School of Science

Author Ahmad Darwish

Title Characterizing Superconducting Resonators in an Autonomous Quantum Heat Engine

Degree programme Science and Technology

Major Quantum Technology

Supervisor Prof. Mikko Möttönen

Advisor M.Sc. Tuomas Uusnäkki

Date 19 September 2025 **Number of pages** 47 **Language** English

Abstract

Quantum heat engines are novel technologies that leverage quantum mechanical principles alongside thermodynamic theory to generate useful work. While experimental realizations of such devices have existed since the 1950s, they require continuous drive by an external control field. Autonomous quantum heat engines offer an alternate approach where the heat engine cycle is driven from within the device itself. Without being superimposed onto an external control field, the generated work from an autonomous quantum heat engine can more easily be observed and extracted. This thesis studies the low-frequency, energy-storing resonator in a superconducting circuit sample proposed as one such autonomous quantum heat engine. Transmission line measurements are performed to characterize the resonator while also analyzing its behavior in the time domain. When thermal-like noise is introduced to the system, the resonance dip is enhanced by up to 4.5 dB. However, the resonator rapidly decays, exhibiting bare resonance behavior after 6 µs without noise. Furthermore, this thesis finds that the intrinsic dissipation rate of the resonator is greater than the photon generation rate of the system. The internal quality factor peaks at 2.1×10^4, higher than the expected values for the type of resonator utilized and four times higher than the bare noiseless resonance. The total quality factor reaches 1.8×10^4 at ideal noise temperatures.

Keywords Autonomous quantum heat engine, circuit quantum electrodynamics, quantum Otto cycle, quantum thermodynamics

Contents

1 Introduction

The twentieth century was marked by significant advancements in quantum physics. Beginning with Planck's discovery of energy quantization, the branch has since become an alternate paradigm in physics. Its associated non-classical phenomena serve as the framework behind potential technologies in fields such as computing [1], sensing [2], and cryptography [3]. On the other hand, thermodynamics is a classical scientific discipline whose practical applications are, in stark contrast, more evident. Of these, heat engines are generally the most prolific; from automotive vehicles [4] to refrigerators [5], their use-cases in society are widespread and significant.

Quantum heat engines (QHE) have long been theorized as a viable technology and have been experimentally demonstrated on several occasions. Similarly to classical heat engines, QHEs transfer heat between hot and cold reservoirs and, in the process, generate power; however, unlike classical systems, this process utilizes quantum mechanical behaviors such as energy quantization, superposition, entanglement, and reversible unitary evolution [6]. The earliest realization of this was a three-level maser presented by Scovil and Schulz-DuBois in 1959 [7]. QHEs have since been experimentally shown in several systems, including spin-½ [8] and single trapped ion systems [9]. However, these engines are driven by a macroscopic control field, which makes it difficult to observe and extract the generated power. Instead, autonomous quantum heat engines (AQHEs) are an alternative platform wherein the process sustains itself without the need for external input.

Therefore, this thesis experimentally studies a potential AQHE implementation based on a quantum harmonic oscillator (QHO) system, i.e., a frequency-tunable QHO coupled to two high-frequency superconducting resonators, which operate as the filtering couplings to the hot and cold reservoirs [10]. In the AQHE, the QHO is realized as a high-frequency superconducting resonator that acts as the working medium of the engine, whose frequency varies between the resonance frequencies of the hot and cold reservoir filters. As the frequency approaches the resonance frequency of one filter, its interaction strength with that filter increases [11]. This process is analogous to the cyclic interaction of the working fluid with the hot and cold baths in a classical heat engine. This high-frequency resonator is also coupled to a low-frequency resonator through optomechanical-like coupling such that usable work can be observed in and extracted from the effective mechanical mode at a lower frequency [10]. To achieve an autonomous operation, the effective optical mode frequency is modulated internally by the mechanical mode through a superconducting quantum interference device (SQUID) [11].

In order to determine the capabilities of the device, it is first essential to study its individual components. This work, therefore, employs transmission lines coupled to the device to characterize the low-frequency, energy-storing environment. Properties, such as resonance frequencies and quality factors, can then be determined by studying the transmission measurements [12]. By analyzing these properties, this work lays the groundwork for future holistic analysis of the device.

This thesis is structured as follows: Sec. 2 covers theoretical concepts relevant to the device. This includes superconducting resonators, quantum thermodynamics,

and optomechanical coupling. Sec. 3 presents the AQHE device and experimental setup, including measurement processes. Sec. 4 reports and discusses the experimental results. Finally, Sec. 5 presents conclusions and future research prospects.

2 Theoretical background

This section presents the theoretical concepts required in realizing and understanding the quantum heat engine. It is organized as follows: the elements of the device are first contextualized individually, then linked based on relevant interaction mechanisms, and finally, their contribution to the heat engine is presented. Sec. 2.1 discusses the relevant circuit architecture for the device by individually introducing each circuit element. Sec. 2.2 builds on this by describing the ways the circuit elements interact with one another through capacitive and optomechanical-like coupling. The means by which this interaction is realized in the device is explained in Sec. 2.3. The section discusses the quantum analog to classical thermodynamics and the Otto cycle, and it relates this information, alongside the previous sections, to the device itself.

2.1 Circuit quantum electrodynamics

Circuit quantum electrodynamics (circuit QED) architecture is the principle for studying light-matter interaction in the quantum regime. Circuit QED involves coupling artificial atoms to quantized electromagnetic fields in order to study their behavior [13]. Mesoscopic devices with atom-like energy spectra, such as non-linear superconducting circuits, behave as artificial atoms [13], and the quantized electromagnetic fields are housed in on-chip resonators operating in the microwave frequency domain [14].

2.1.1 Superconducting Circuits

Superconducting circuits are a crucial platform for observing non-classical phenomena and are a core component of circuit QED. Generally, preparing a system in the quantum regime requires that the following condition holds: $\hbar\omega \gg k_B T$ [6]. In other words, the energy quantum of the system $\hbar\omega$ must be much greater than its characteristic thermal energy $k_B T$. This ensures that thermal excitations in the system are well suppressed [6]. Alongside thermal excitations, decoherence also steers the system towards the classical regime [15]. The primary sources of decoherence are the design of the circuit and its coupling to the environment [16], [17]. The environment primarily consists of the surrounding electromagnetic field, control equipment, and measurement devices; coupling to the environment can, therefore, be reduced by appropriately modifying the measurement setup [6]. For instance, component losses are caused by resistance in the conductors that form the circuit. This source of loss can be completely suppressed by utilizing superconducting circuits [6].

Below a critical temperature T_c, certain materials act as superconductors. These temperatures give rise to BCS instability, where pairs of valence electrons are stably bound as particles called Cooper pairs; phonons in the conductor mediate this attraction. While electrons are fermions, Cooper pairs are composite bosons, which are capable of simultaneously occupying the same quantum state. Therefore, Cooper pairs can form a macroscopic quantum state by occupying the same state. This condensate-like state is insensitive to impurities in the material and thus, flows unimpeded. Cooper

pairs make it possible for superconductors to exhibit the following special properties: zero resistance, persistent currents, quantized flux in a loop, and no internal magnetic fields (i.e., the Meissner effect) [18].

The temperature at which the quantum regime condition $\hbar\omega \gg k_B T$ holds is, in most cases, less than the critical temperature of a conductor. For typical microwave frequencies in a quantum circuit, $\omega = 2\pi \times 6\,\text{GHz}$, the quantum regime condition holds for temperatures well below 400 mK. On the other hand, the critical temperature T_c of niobium, a commonly utilized conductor in quantum circuits, is 9.25 K [19]. As this temperature is significantly above that which is required for non-classical behavior, superconductivity emerges as a consequential by-product of operating a circuit in the low-temperature environment necessary to fulfill the quantum regime condition. The properties exhibited by superconductors reduce loss and lay the groundwork for certain non-linear circuit elements, both of which are necessary in circuit QED architecture. With no resistance, superconductivity suppresses a major intrinsic source of component loss, which increases the coherence time of the quantum system [6]. Furthermore, the quantization of flux across a superconducting loop is a key property of SQUIDs, a non-linear inductor, which in this work is a key component in the autonomous modulation of the optical mode frequency.

2.1.2 Lumped quantum LC oscillator

In order to develop sufficient intuition for the role of quantum LC (inductor-capacitor) oscillators in the device, this subsection begins by individually introducing each component. This is possible due to the lumped element model, which simplifies electric circuits by treating their components as individual, separable devices. Components are assumed to be connected with instantaneous and lossless wires. This approximation is valid, with no loss of accuracy, when the spatial dimensions of the components are much smaller than the wavelength of the circuit [13].

An inductor is a passive circuit element that stores energy in its magnetic field and is typically composed of coiled conducting wires. It operates based on the following principle: current through the inductor produces a magnetic field around it, a changing current results in a changing magnetic field, and a changing magnetic field induces voltage across the inductor (i.e., Faraday's Law) [20]. Therefore, a voltage across an inductor is proportional to the rate of change of current. For linear inductors, this can be formalized in the following relation: $V(t) = L\,\mathrm{d}I/\mathrm{d}t$ [21]. L is inductance, which measures the extent to which an inductor opposes a change in current. From this relation, it can be ascertained that an inductor has no voltage across it when the current through it is constant. In this case, the inductor behaves as a short-circuit element.

Hereafter, it is therefore assumed that the signal flowing through the circuit is alternating (AC) and can be expressed sinusoidally in phasor form: $X = X_0 \cos(\omega t + \phi_X) = \Re(X_0 e^{i\omega t} e^{i\phi_X})$, where X_0 is the signal amplitude, $\omega = 2\pi f$ is the angular frequency, and ϕ_X is the signal phase [22]. Phasor X_ϕ is defined as $X_\phi := X_0 e^{i\phi_X}$; the phasor of the time derivative, $\dot{X} = \Re(i\omega X_0 e^{i\omega t} e^{i\phi_X})$, is $i\omega X_0 e^{i\phi_X} = i\omega X_\phi$ [22]. Therefore, the phasor of the current flowing through an inductor is $I_\phi := I_0 e^{i\phi_I}$. Combining this with the voltage-current relation of an inductor, the voltage phasor is

derived: $V_\phi := \mathrm{i}\omega L I_0 e^{\mathrm{i}\phi_I} = \mathrm{i}\omega L I_\phi$. The phasor form generally simplifies computation; for example, impedance Z can be calculated as $Z = V_\phi / I_\phi$, where V_ϕ and I_ϕ are phasors [22]. In the case of the inductor,

$$Z_\mathrm{L} = \mathrm{i}L\omega. \tag{1}$$

Impedance is defined as $Z = R + \mathrm{i}X$ and is represented in the units of Ohms (Ω), where R is resistance and X is reactance [21]. Therefore, an ideal inductor has no resistance, and its impedance is purely imaginary, with it entirely derived from reactance.

On the other hand, a capacitor is a passive circuit element that stores energy in its electric field, and it is typically composed of two parallel conducting plates separated by a dielectric [21]. Charges of opposite sign accumulate on the opposite plates, which results in a potential difference between the conductors [21]. For linear capacitors, this is defined by the following relation: $V = Q/C$, where Q is the charge built up on one plate and C is the capacitance, which measures the ability of the capacitor to store charge [20]. As current is defined as $I(t) = \mathrm{d}Q/\mathrm{d}t$, it is then possible to rewrite the voltage-charge relation as a voltage–current relation: $I(t) = C\,\mathrm{d}V/\mathrm{d}t$. For there to be some current flowing through the capacitor, the voltage across it must be non-constant. As with the inductors, it is assumed that the signal is alternating and harmonic. Employing the phasor representation for voltage, $V_\phi := V_0 e^{\mathrm{i}\phi_V}$, it is possible to define the phasor for current through the capacitor as $I_\phi := \mathrm{i}\omega C V_0 e^{\mathrm{i}\phi_V} = \mathrm{i}\omega C V_\phi$. Therefore, capacitors have impedance

$$Z_C(\omega) = \frac{1}{\mathrm{i}\omega C}. \tag{2}$$

As with an ideal inductor, an ideal capacitor is non-dissipative, and its impedance is imaginary, with it entirely derived from reactance.

An LC oscillator consists of an inductor of inductance L and a capacitor of capacitance C as shown in Fig. 1(a). In the system, energy oscillates between the

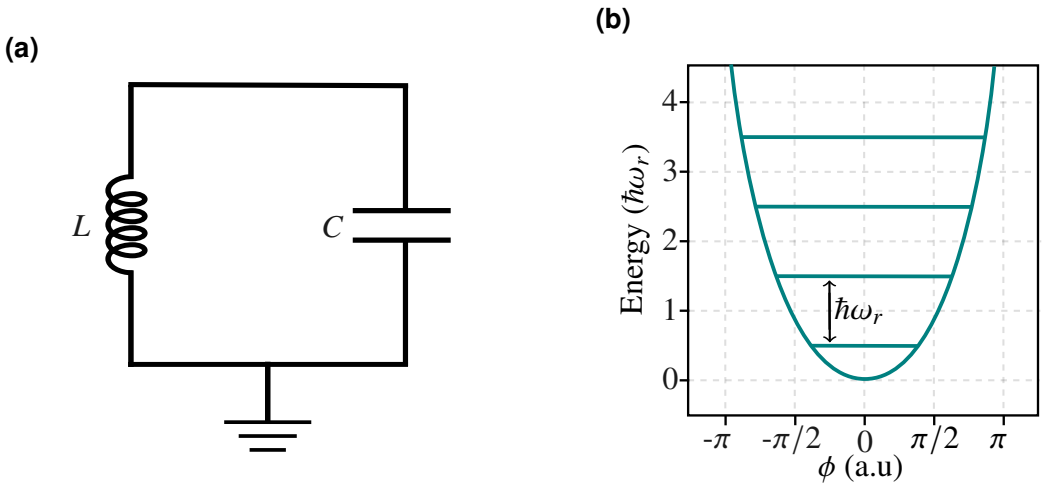

Figure 1: (a) Lumped LC oscillator circuit diagram. (b) Energy levels of an LC oscillator.

electric energy in the capacitor and the magnetic energy in the inductor [23]. The resonance frequency for LC circuits is generally defined as the frequency at which the reactance of the capacitor and inductor are equal and cancel each other out [23]. From equations (1) and (2), it can easily be found that the resonance frequency of the circuit is

$$\omega_{\mathrm{r}} = \frac{1}{\sqrt{LC}}. \tag{3}$$

At this frequency, total impedance for series circuits, $Z_{\text{series}} = Z_{\mathrm{L}} + Z_{\mathrm{C}}$, is zero; whereas total impedance, $Z^{-1}_{\text{parallel}} = Z^{-1}_{\mathrm{C}} + Z^{-1}_{\mathrm{L}}$, is infinite for parallel circuits. Therefore, series LC circuits maximally store energy at resonance, with them behaving as band-pass filters with maximum response around ω_{r}. On the other hand, for parallel LC circuits, the system behaves as a band-stop filter with minimum response at resonance.

Additionally, the circuit can also be characterized by its quality factor, i.e., the ratio of energy stored to energy dissipated in one cycle [23]. A higher quality factor indicates that the circuit stores energy more efficiently and, accordingly, has a sharper peak [23]. In the case of an LC oscillator, the quality factor is

$$Q = \frac{\omega_r}{\kappa}, \tag{4}$$

where ω_r is the resonance frequency defined in Eq. (3) and κ is the oscillator linewidth, i.e., its full width at half maximum.

Thus far, the discussion has primarily revolved around the classical properties of a lumped LC circuit. Instead, an analysis of its quantum analog is necessary to properly understand the way it is utilized in quantum systems. Properties, such as resonance frequency and quality factor, are for the most part unchanged when investigating LC oscillators in the quantum regime. Instead, quantization of energy sets the two systems apart, and the quantum LC oscillator with discretized energy levels operates as a QHO [24], [25]. To begin, magnetic flux through an inductor, Φ, is related to current and inductance by the following relation: $\Phi(t) = LI(t)$. More generally, Lenz's Law relates magnetic flux to voltage by $\dot{\Phi} = V$. Power is generally defined as $P = VI$ while its time integral $E(t) = \int_{-\infty}^{t} V(t')I(t')\mathrm{d}t'$ is energy. Applying this formula alongside the voltage-current relation for capacitors, the electric energy stored in a capacitor is

$$T = \int_{-\infty}^{t} VC\dot{V}\,\mathrm{d}t' = \frac{1}{2}CV^2 = \frac{1}{2}C\dot{\Phi}^2. \tag{5}$$

$t = -\infty$ is assumed to be a point significantly far back in time such that the system had zero voltage and zero current. Furthermore, the electric energy stored in the capacitor is classified as the kinetic energy of the system. This association is based on the $\dot{\Phi}$ term, analogous to velocity in a classical system: $T = mv^2/2 = m\dot{q}^2/2$. Therefore, the magnetic energy stored in the inductor is interpreted as potential energy,

$$U = \int_{-\infty}^{t} L\dot{I}I\,\mathrm{d}t' = \frac{1}{2}LI^2 = \frac{1}{2L}\Phi^2. \tag{6}$$

The generalized coordinate and velocity are set as Φ and $\dot{\Phi}$, respectively. The Lagrangian of the system, $\mathcal{L}$, and canonical momentum, p, can then be formalized as

$$\mathcal{L} = T - U = \frac{1}{2}C\dot{\Phi}^2 - \frac{\Phi^2}{2L}, \tag{7}$$

$$p \equiv \frac{\partial L}{\partial \dot{\Phi}} = C\dot{\Phi} = Q. \tag{8}$$

Before formulating the classical Hamiltonian, the Euler-Lagrange equation is applied to determine that the natural oscillating frequency of the system is indeed $\omega = 1/\sqrt{LC}$, which matches that of Eq. (3),

$$\begin{aligned} \frac{\partial \mathcal{L}}{\partial \Phi} - \frac{\mathrm{d}}{\mathrm{d}t}\frac{\partial \mathcal{L}}{\partial \dot{\Phi}} &= 0, \\ \frac{\Phi}{LC} + \ddot{\Phi} &= 0, \end{aligned} \tag{9}$$

where Φ is selected as generalized position and Q as generalized momentum. Using these definitions, the Legendre transformation, $\mathcal{H}(p,q) \equiv \dot{q}p - \mathcal{L}(\dot{q},q)$, converts the Lagrangian to a Hamiltonian,

$$\mathcal{H}(Q,\Phi) = Q\dot{\Phi} - \left(\frac{C\dot{\Phi}^2}{2} - \frac{\Phi^2}{2L}\right) = \frac{Q^2}{2C} + \frac{\Phi^2}{2L}. \tag{10}$$

Quantizing the Hamiltonian involves promoting the generalized position and momentum terms, Φ and Q, to canonical operators, $\hat{Q}$ and $\hat{\Phi}$, that satisfy the canonical commutation relation,

$$[\hat{\Phi}, \hat{Q}] = \mathrm{i}\hbar. \tag{11}$$

Therefore, the quantum Hamiltonian can be written as follows,

$$\hat{\mathcal{H}} = \frac{\hat{Q}^2}{2C} + \frac{\hat{\Phi}^2}{2L} = \frac{\hat{Q}^2}{2C} + \frac{1}{2}C\omega_\mathrm{r}^2\,\hat{\Phi}^2. \tag{12}$$

To observe discretized harmonic behavior, creation and annihilation operators, $\hat{a}^\dagger$ and $\hat{a}$, are introduced and related to flux and charge. These operators satisfy the following commutation relation: $[\hat{a}, \hat{a}^\dagger] = 1$. Therefore, flux and charge operators are defined as follows,

$$\begin{aligned} \hat{\Phi} &= \sqrt{\frac{\hbar}{2C\omega_\mathrm{r}}}\left(\hat{a} + \hat{a}^\dagger\right) = \Phi_\mathrm{zpf}\left(\hat{a} + \hat{a}^\dagger\right), \\ \hat{Q} &= \mathrm{i}\sqrt{\frac{\hbar C\omega_\mathrm{r}}{2}}\left(\hat{a} - \hat{a}^\dagger\right) = \mathrm{i}Q_\mathrm{zpf}\left(\hat{a} - \hat{a}^\dagger\right), \end{aligned} \tag{13}$$

where Φ_zpf and Q_zpf are the zero-point fluctuations of flux and charge, respectively. It follows from Eq. (13) that Eq. (12) simplifies to

$$\hat{H} = \hbar\omega_\mathrm{r}\left(\hat{a}^\dagger\hat{a} + \frac{1}{2}\right). \tag{14}$$

As $\hat{a}^\dagger \hat{a} = \hat{n}$, where $\hat{n}$ is an operator whose eigenvalues n are the number of photons in the system with energy $\hbar\omega_r$ [13]. Eq. (14) demonstrates that the total energy in the system is discretized by the number of photons. Furthermore, Eq. (14) matches that of a QHO with eigenvalues $\hbar\omega_r\,(n + 1/2)$ as is shown in Fig. 1b. The QHO has equidistant spacing $\hbar\omega_r$ between energy levels, and $\hat{a}$ shifts the energy eigenvalue down by $\hbar\omega_r$ and $\hat{a}^\dagger$ shifts it up by the same amount [26]. This can be thought of as moving up and down the energy ladder shown in Fig. 1(a). Moreover, the energy eigenvalue for $n = 0$, $E_0 = \hbar\omega_r/2$ is called the zero-point energy, indicating that the system maintains some energy without the presence of photons of energy $\hbar\omega_r$.

2.1.3 Coplanar waveguide resonator

As the circuit wavelength becomes comparable to the spatial dimension of its components, the lumped element model no longer becomes accurate [27]. Instead, distributed circuit representation must be used to model the system [28]. This model assumes that properties, such as resistance, inductance, and capacitance, are distributed throughout the circuit [27]. Components are assumed to be infinitesimally small and that the wires connecting them are imperfect. Furthermore, unlike the lumped element model, the phase and magnitude of both voltage and current vary throughout the device [28]. This model is particularly relevant for transmission lines, cables designed to contain and conduct electromagnetic fields [6]. Fig. 2 is an approximate lumped model representation of a single section of these cables. As is shown in the figure, a transmission line is formed of two conductors separated by some dielectric insulator, where L' is the per unit length self-inductance and C' is the per unit length capacitance caused by their proximity [28]. A transmission line may also have per unit length conductance G' and resistance R'. G' represents dielectric loss and R' represent conductor loss [28]. As was discussed in Sec. 2.1.1, superconductors are lossless and thus R' is, onward, taken as 0; similarly, it is assumed that the dielectric is lossless and thus, G' is also, onward, set as 0. A transmission line can be roughly interpreted as repeated iterations of the section shown in Fig. 2 [6].

Using Kirchhoff's laws and setting $\Delta x \to 0$, the Telegrapher equations can be

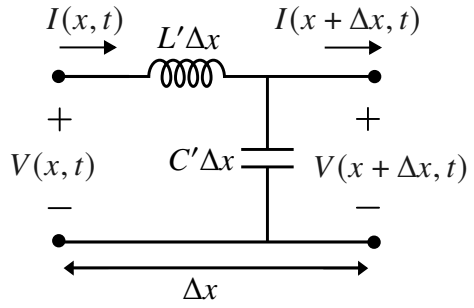

Figure 2: Lumped element model of a lossless transmission line.

derived.

$$\begin{aligned} \frac{\partial V(x,t)}{\partial x} &= -L' \frac{\partial I(x,t)}{\partial t}, \\ \frac{\partial I(x,t)}{\partial x} &= -C' \frac{\partial V(x,t)}{\partial t}. \end{aligned} \tag{15}$$

Upon solving with the sinusoidal steady-state condition, they yield the following general solutions for voltage and current

$$\begin{aligned} V(x) &= V_0^+ e^{-i\omega\sqrt{L'C'}x} + V_0^- e^{i\omega\sqrt{L'C'}x}, \\ I(x) &= I_0^+ e^{-i\omega\sqrt{L'C'}x} + I_0^- e^{i\omega\sqrt{L'C'}x}. \end{aligned} \tag{16}$$

The space-dependent wave equations (16) reveal that transmission lines are indeed distributed parameter networks wherein the phase and magnitude of voltage and current vary along the wire.

The specific orientation and design of the two conductors can vary; for the most part, however, the operating principle stays the same. For example, rather than two parallel wires, coaxial cables consist of an inner conducting wire confined within dielectric material itself surrounded by an outer conducting shield [28]. The electromagnetic field is confined in the space between the outer and inner conductors. Furthermore, transmission lines can also be fabricated directly on printed circuit boards. These transmission lines are called planar transmission lines, consisting of flat conducting strips atop some dielectric material [28]. Of these, coplanar waveguides (CPWs) kickstarted early research into cQED and have since become a key component in the field [29].

A CPW, as illustrated in Fig. 3(a), is composed of three conductors of thickness T printed atop a dielectric substrate and separated by distance S to two ground planes on either side [14]. The center conductor is of length D and is capacitively coupled to the return conductors at each end. Signals are transmitted by the planar structure in a similar way to other transmission lines, such as coaxial cables [13]. Fig. 3(a), a cross-section of the CPW, illustrates how electromagnetic field lines are approximately

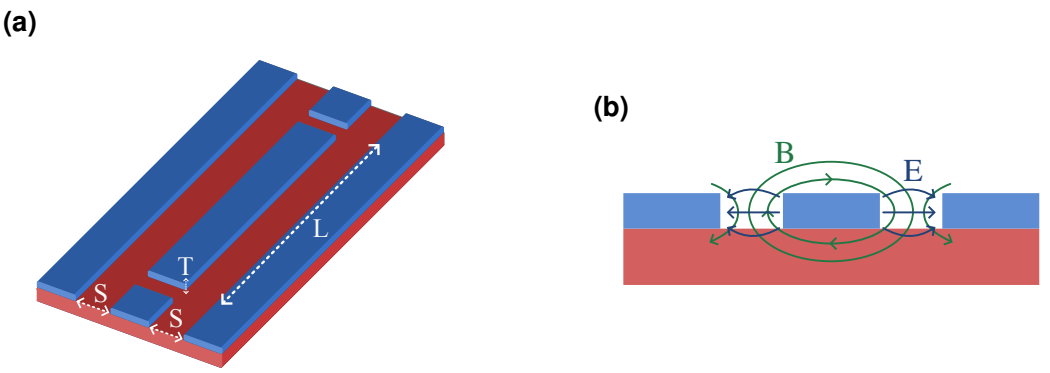

Figure 3: (a) Schematic of a coplanar waveguide resonator. (b) Schematic diagram of the electric and magnetic field lines of a coplanar waveguide resonator.

confined between the center conductor plane and the ground planes on either side. A CPW's behavior can be manipulated by adjusting its geometry in fabrication, which, in turn, imposes certain boundary conditions on the device. As a result of these boundary conditions, the signal is discretized into a set of electromagnetic modes, each with a distinct frequency [13]. For example, in Fig. 3(a), the white cosine-shaped lines above the center conductor represent the second mode function. Certain boundary conditions also introduce resonator behavior in the waveguide. The zero current boundary condition, achieved by shorting an endpoint via a gap in the conductor, is one such boundary condition; zero voltage is another condition, and can be achieved by grounding an endpoint [13]. However, Fig. 3(a) is that of a CPW with open boundaries on either end of the center conductor. Such a CPW resonator is called a $\lambda/2$ resonator and has fundamental frequency f_0 and harmonics f_n [13],

$$f_0 = \frac{1}{L'C'}\frac{1}{2D}\,, \quad f_n = (n+1)\,f_0\,. \tag{17}$$

L' and C' are, respectively, inductance and capacitance per unit length.

Several considerations are made to ensure that the CPW resonator operates in a low-to-no-loss regime. The first, as was discussed in Sec. 2.1.1, is to use superconducting material. The second is to select a dielectric with a low-loss tangent, such as silicon [30]. Generally, losses in the CPW resonator can be described by the mode quality factor Q_n, differing slightly from that of Eq. (4). Instead, frequency ω_r is substituted with ω_n and linewidth κ with κ_n. Internal losses in the CPW, i.e., coupling to uncontrolled degrees of freedom, are often distinguished from external losses, i.e., coupling to the input and output ports [13]. In terms of quality factor, this distinction is accordingly expressed:

$$Q_{\mathrm{L},n}^{-1} = Q_{\mathrm{int},n}^{-1} + Q_{\mathrm{ext},n}^{-1}\,, \tag{18}$$

where $Q_{\mathrm{L},n}$ is the loaded mode quality factor. Through careful fabrication, the internal quality factor, $Q_{\mathrm{int},n}$, can be improved by, for example, reducing two-level systems (TLS) in the dielectric [13]. The external quality factor, $Q_{\mathrm{ext},n}$, can be altered by adjusting the center conductor's capacitive coupling with the return conductors [14]. As a result of its tunability, the resonator can be over- or under-coupled, changing how it behaves. This is particularly important for systems where characteristics, such as coherence times or fast readout, are valued. For fast read out, over coupling, i.e., $Q_{\mathrm{ext},n} \ll Q_{\mathrm{int},n}$, is preferred. Whereas, for longer photon storage times, under coupling, i.e., $Q_{\mathrm{ext},n} \gg Q_{\mathrm{int},n}$, is required [13]. In the latter case, energy dissipation is generally limited only by internal losses, which, as aforementioned, can be significantly reduced in fabrication [13].

2.1.4 Non-linear superconducting circuit elements

Central to circuit QED architecture are non-linear circuit elements, which serve as an important tool in artificial atom fabrication by introducing anharmonicity between energy levels [26]. In the context of the AQHE, and as discussed in more detail in Sec. 2.3.3, these non-linear elements are needed for the autonomous operation of the device [11].

Figure 4: Circuit diagram symbol of a Josephson junction

A Josephson junction is a non-linear inductor commonly used in superconducting circuits and is often represented in circuit diagrams by the symbol shown in Fig. 4. It consists of two superconductors separated by a thin insulating layer, through which Cooper pairs tunnel [6]. The Josephson effect states that, for a given Josephson junction, there is a critical current I_c below which all current flows without voltage across the junction [31]. Instead, current through a Josephson junction and voltage across it are

$$\begin{aligned} I &= I_c \sin\varphi \,, \\ V &= \frac{\Phi_0}{2\pi}\frac{\mathrm{d}\varphi}{\mathrm{d}t} \,, \end{aligned} \tag{19}$$

where $\varphi = \phi_1 - \phi_2$ is the gauge-invariant phase difference across the junction, and $\Phi_0 = h/2e$ is the flux quantum [32], [33]. Combining Eq. 19 yields

$$\frac{\mathrm{d}I}{\mathrm{d}t} = (I_c \cos\varphi)\left(\frac{2\pi}{\Phi_0}V\right) \,. \tag{20}$$

As voltage is proportional to the rate of change of current, the equation indeed describes an inductor [32]. It is, therefore, possible to define a Josephson inductance using the conventional inductor relation $V = L\dot{I}$ [32]:

$$L_J = \frac{\Phi_0}{2\pi I_c \cos\varphi} \,. \tag{21}$$

The same relations presented in Eq. (19) can also be used to derive the energy of the Josephson junction [6]:

$$E = -\frac{\Phi_0 I_c}{2\pi}\cos\left(\frac{2\pi}{\Phi_0}\varphi\right) = -E_J \cos\left(\frac{2\pi}{\Phi_0}\varphi\right) . \tag{22}$$

In Eq. 22, $E_J = \Phi_0 I_c/2\pi$ is called Josephson energy. While Eq. 22 accounts for the inductive term, there is also some capacitive contribution due to the charge build-up at each superconducting end. In circuit diagrams, the capacitive contribution is usually captured by some non-existent capacitor of capacitance C_J drawn in parallel with the junction [6].

In quantum circuit design, Josephson junctions are most often utilized in SQUID loops, making use of the Josephson effect and flux quantization. While there are many possible arrangements for a SQUID loop, one commonly used is that of two Josephson junctions arranged in parallel, named the direct current (DC) SQUID. This is the arrangement used in the quantum heat engine sample and thus is the focus of this section. A circuit diagram of this specific arrangement is shown in

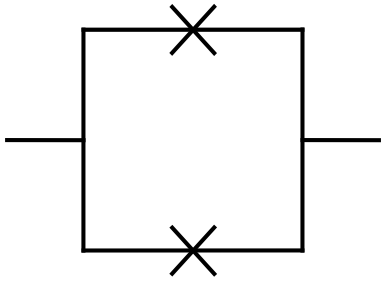

Figure 5: Circuit diagram of a DC SQUID loop

Fig. 5. It is a requirement that, for superconducting loops, the wavefunction describing the condensate-like state be single-valued [34]. In other words, the phase of the wavefunction must return to the same value after a full loop. For loops threaded by some magnetic flux, the following, therefore, must hold [34],

$$\oint \nabla\phi \cdot \mathrm{d}\mathbf{l} = 2\pi n. \tag{23}$$

It then follows that, in the superconducting region, the magnetic flux is quantized as [35]

$$\Phi = n\Phi_0, \tag{24}$$

where n is an integer and Φ_0 is the flux quanta as previously defined. This property is derived in more detail in [36]. As shown in Eq. (23) and (24), flux quantization relates phase in a superconducting loop to the external magnetic flux threading it. A SQUID is one such superconducting loop, and thus, the relation also holds true for it; more specifically, $2\pi\Phi_{\text{ext}}/\Phi_0 = \varphi_2 - \varphi_1$, where $\varphi_{1/2}$ is the phase difference across each of the Josephson junctions [34]. As the current through a Josephson junction is dependent on the phase difference across it, the current flowing through a SQUID depends on the magnetic flux threading the loop. This dependency is formalized as

$$I_{\text{c}} = 2I_0 \cos\frac{\pi\Phi_{\text{ext}}}{\Phi_0}, \tag{25}$$

with Φ_{ext} as external flux, I_0 as the critical current of each of the two identical Josephson junctions, and Φ_0 as the magnetic flux quantum [34]. Eq. (25) reveals that the critical current of a DC SQUID can be modulated by applying an external flux. The DC SQUID, therefore, can behave as a magnetometer, capable of detecting magnetic fields with a high degree of sensitivity [37]. Similarly, Josephson induction depends on phase, and as a result, the inductance of a SQUID can also be modulated by an external magnetic field. This is evident from Eq. (21). In other words, SQUIDs also behave as tunable, non-linear inductors [34].

2.2 Resonator coupling

Coupling between circuit elements plays an integral role in the operation of the AQHE. Capacitors couple the hot and cold filters to the system. SQUID coupling is

responsible for transferring photons between the different frequency environments. Finally, optomechanical-like coupling between the same two resonators mediates the autonomous operation of the system. This section explores these relations, taking a general approach without specifically referencing the AQHE environment.

2.2.1 Capacitive resonator coupling

Capacitive coupling between resonators is achieved by splitting two resonators with a capacitor of some capacitance C_g. Mediated by changes in the electric field between the resonators, capacitive coupling enables energy exchange through the flow of displacement current [38]. Oscillating signals are required for this exchange; capacitive coupling, therefore, isolates the DC signal [39].

The theoretical model for capacitive coupling between quantum LC oscillators is expressed by the Hamiltonian [40]

$$\mathcal{H} = \hbar\omega_{\mathrm{a}}\hat{a}^{\dagger}\hat{a} + \hbar\omega_{\mathrm{b}}\hat{b}^{\dagger}\hat{b} + \hbar g\left(\hat{a}\hat{b}^{\dagger} + \hat{a}^{\dagger}\hat{b}\right). \tag{26}$$

Equation 26 consists of individual resonator energy terms along with the interaction term $\hbar g(\hat{a}\hat{b}^{\dagger} + \hat{a}^{\dagger}\hat{b})$. Having applied the rotating wave approximation, fast rotating terms have been dropped [40]. The interaction term describes the coherent transfer of photons between the resonators, with g denoting the coupling strength.

Interaction between the two resonators is strongest when detuning, i.e., $\Delta = \omega_a - \omega_b$, is zero [40]. When this is the case, energy, in the form of photons, is maximally exchanged. The directionality of this exchange is dependent on several factors, one of which is the initial state of the system. As photons cannot be emitted when at ground state, the term $\hat{a}^{\dagger}\hat{b}$ from Eq. 26 has no effect when, for example, resonator B is at ground state. Therefore, if one resonator is initially at the ground state and the other is excited, photons naturally flow from the excited to the unexcited resonator.

2.2.2 Optomechanical coupling

Cavity optomechanics involves studying the interaction between electromagnetic radiation and mechanical systems using optical cavities and mechanical resonators [41]. Non-linear coupling between the optical and mechanical elements of an optomechanical system enables momentum exchange, typically mediated by means of radiation pressure or modulating boundaries [41]. A schematic model of an optomechanical system is shown in Fig. 6.

By coupling two superconducting microwave resonators to one another with a SQUID, it is possible to produce a non-linear interaction similar to that of standard optomechanical coupling. This setup, illustrated in Fig 7 is a cQED analogue of standard optomechanical systems and abides by the same general principle: the quadrature of one of the resonators couples to the photon number of the other [42]. The Hamiltonian of the system is represented as

$$\mathcal{H} \approx \hbar\omega_{\mathrm{A}}\hat{a}^{\dagger}\hat{a} + \hbar\omega_{\mathrm{B}}\hat{b}^{\dagger}\hat{b} - \hbar g_0\hat{a}^{\dagger}\hat{a}(\hat{b} + \hat{b}^{\dagger}), \tag{27}$$

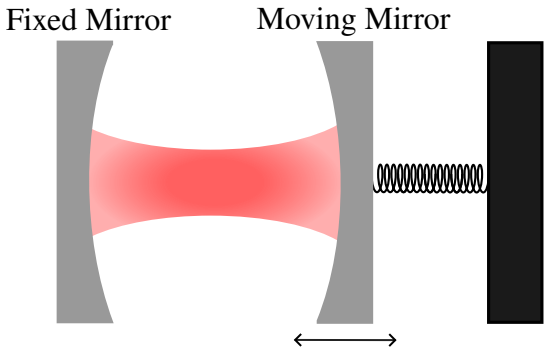

Figure 6: Schematic of an optical cavity coupled to a mechanical resonator.

where $\omega_{A/B}$ are the resonance frequencies, $\hat{a}/\hat{b}$ and $\hat{a}^\dagger/\hat{b}^\dagger$ are the annihilation and creation operators of the optical/mechanical modes, respectively, and g_0 is the coupling strength between resonator A and B [42]. In the interaction term $-\hbar g_0 \hat{a}^\dagger \hat{a}(\hat{b} + \hat{b}^\dagger)$, coupling strength is defined as

$$g_0 = \omega_A F(\Phi^0_{ext}) G_1, \tag{28}$$

where $F(\Phi_{ext})$ is a factor that depends on the properties of the SQUID and the external flux threading it, and G_1 is a factor that depends on the geometry of the SQUID loop and the resonators [42]. As discussed in Sec. 2.1.4, a SQUID is a tunable non-linear inductor [34]. By embedding it in a resonator, the magnetic flux that threads it modulates the inductance of the resonator and, accordingly, the resonance frequency [42]. Using Fig. 6 for reference, this is analogous to modulating the position of the mirror in the optical cavity. However, to properly liken this setup to that of an optomechanical system, changes in the boundary conditions of one resonator must be mediated by the dynamic behavior of the other [42]. Recalling 2.1.3, this can be achieved by exploiting the magnetic field of the other resonator in such a way that

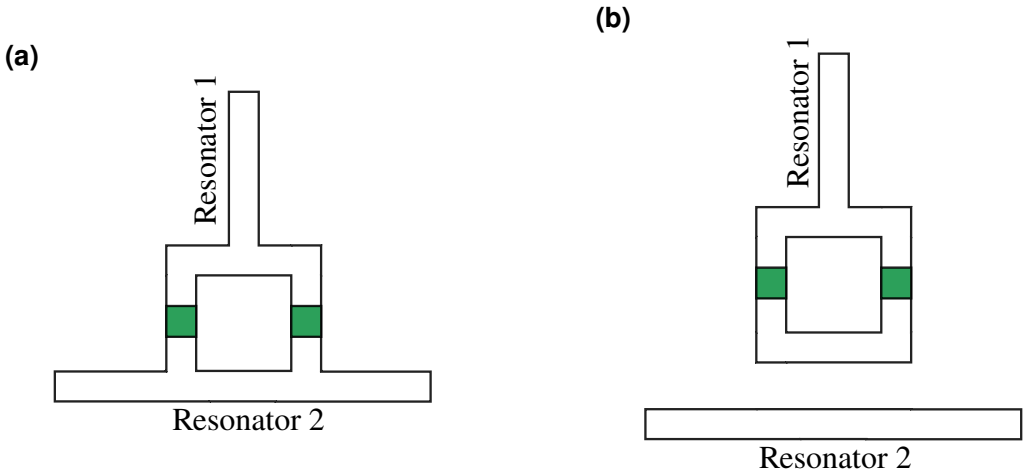

Figure 7: (a) Schematic model of the galvanic coupling geometry (b) Schematic model of the inductive coupling geometry.

it threads the SQUID loop. It can be shown, as is done in [42], that the effective Hamiltonian of such a system is of standard optomechanical form.

The setup can be realized in two ways: inductive coupling and galvanic coupling. Both are illustrated in Fig. 7 with the green sections representing Josephson junctions. In either geometry, it is possible to adjust the interaction strength by applying an external flux bias. By tuning flux bias, it is, therefore, possible to move between strong and weak coupling regimes, adding an additional degree of freedom [42]. This is in contrast to standard optomechanical systems wherein coupling strength is generally fixed, being determined by setup design [41].

2.3 Quantum heat engine theory

While classical thermodynamics is generally concerned with a phenomenological understanding of macroscopic systems, quantum thermodynamics seeks to synthesize classical thermodynamic theory with the dynamics of quantum systems. By utilizing tools from statistical mechanics, a quantum equivalent to classical thermodynamic descriptions is presented, culminating to a comprehensive theoretical framework that is used to analyze the thermodynamics of quantum systems. This section explores this framework and presents quantum equivalents to the Otto cycle and heat engines. In addition, a brief theoretical description of the AQHE device is given, incorporating relevant theory from Sec. 2.1 and Sec. 2.2.

2.3.1 Thermodynamic description of quantum systems

In quantum thermodynamics and statistical mechanics, systems are described by a density matrix, capable of representing both pure, well-defined, and mixed, non-well-defined states. Density matrices are, therefore, capable of effectively describing how quantum systems interact with their environment, a necessary prerequisite for quantum thermodynamics [43]. For quantum heat engines, quasi-static operation is generally required in order to maximize efficiency; this is particularly relevant for the Otto-like cycle implemented in the AQHE device [44], [45]. Quasi-static processes are processes in which the system evolves in such a way that it is constantly in equilibrium. It is further assumed that, for these processes, the quantum system's dynamics can be characterized by a parametrized Hamiltonian $\hat{\mathcal{H}}(\lambda)$ where λ is some control parameter [46]. Equilibrium states of the quantum system are, therefore, given by the following Gibbs state density operator

$$\hat{\rho}_{\mathrm{G}} = \frac{e^{-\beta\hat{\mathcal{H}}(\lambda)}}{Z}, \tag{29}$$

where $Z = \mathrm{Tr}\{e^{-\beta\hat{\mathcal{H}}}\}$ is the partition function and $\beta = 1/k_{\mathrm{B}}T$ is the inverse temperature. Quasi-static processes mandate that each stage of the system's evolution can be described by one such Gibbs state, the thermodynamic entropy of which is given by [46]

$$S = -\mathrm{Tr}\{\hat{\rho}_{\mathrm{G}} \ln \hat{\rho}_{\mathrm{G}}\} = \beta\,(E - F)\,. \tag{30}$$

In Eq. (30), $E = \mathrm{Tr}\{\hat{\rho}_\mathrm{G}\hat{\mathcal{H}}\}$ is internal energy and $F = -1/\beta \ln Z$ is the Helmholtz free energy [46]. To understand energy exchange in quantum thermodynamics, the isothermic condition is considered. For such processes, change in entropy is

$$\mathrm{d}S = \beta\left(\mathrm{Tr}\{\mathrm{d}\hat{\rho}_\mathrm{G}\hat{\mathcal{H}}\} + \mathrm{Tr}\{\hat{\rho}_\mathrm{G}\mathrm{d}\hat{\mathcal{H}}\} - \mathrm{d}F\right) = \beta\mathrm{Tr}\{\mathrm{d}\hat{\rho}_\mathrm{G}\hat{\mathcal{H}}\}. \tag{31}$$

As is the case with classical thermodynamics, heat is the change of the internal energy of a system due to entropy. While work is also a change in internal energy, it emerges due to changes in the Hamiltonian. Therefore, the following can be concluded about energy exchange,

$$\mathrm{d}E = \mathrm{d}Q + \mathrm{d}W \equiv \mathrm{Tr}\{\mathrm{d}\hat{\rho}_\mathrm{G}\hat{\mathcal{H}}\} + \mathrm{Tr}\{\hat{\rho}_\mathrm{G}\mathrm{d}\hat{\mathcal{H}}\}. \tag{32}$$

For quasistatic processes, therefore, the following holds,

$$\begin{aligned} \mathrm{d}S &= \beta\,\mathrm{d}Q, \\ \mathrm{d}F &= \mathrm{d}W. \end{aligned} \tag{33}$$

As a result, energy change in quasistatic processes is split into entropic cost, from the $\mathrm{d}S$ term, and useful work, from the $\mathrm{d}F$ term [46].

2.3.2 Quantum Otto cycle

Classically, the Otto cycle consists of four strokes, i.e., thermodynamic processes, that transform the system between equilibrium states A, B, C, D. Between A and B, the system is adiabatically compressed, i.e., with no heat exchange with its surroundings, the volume of the system decreases and its temperature increases [46]. From B to C, the system undergoes isochoric heating, wherein the system, with constant volume,

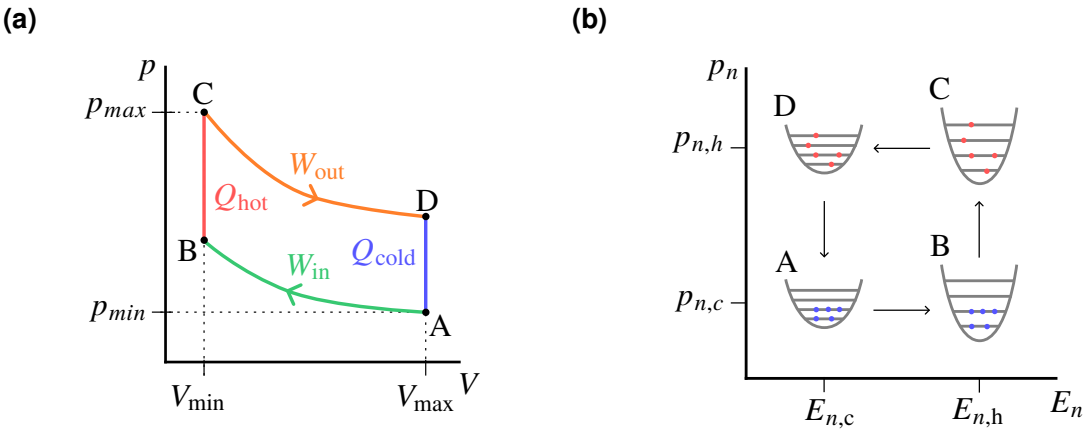

Figure 8: (a) Pressure-volume diagram of the classical Otto cycle. Illustrated are the four different thermodynamic strokes alongside the energy change associated with each. (b) Population-energy illustration of the quantum Otto cycle.

increases its temperature by exchanging heat with a hot bath [46]. The process from C to D is adiabatic expansion, i.e., with no heat exchange with the environment, the volume of the system increases and its temperature decreases [46]. Finally, the system isochorically cools from D to A, i.e., the volume of the system is kept constant while the temperature of the system reduces due to coupling with a cold bath [46]. Entropy remains constant during the two adiabatic strokes and thus, the energy change is entirely a result of inputted and outputted work. On the other hand, energy change during the isochoric processes is entirely entropic and is determined by the heat exchanged with the hot and cold baths ($\mathrm{d}S = \beta\ \mathrm{d}Q$). As shown in Fig. 8(a), the cycle can be illustrated by a pressure-volume (pV) diagram. Realizing thermodynamic cycles in quantum systems involves redefining the aforementioned processes. In the quantum regime, isochoric processes require that the energy level population is changed until the system is in equilibrium with a heat reservoir [46]. As the energy eigenvalues stay the same, quantum isochoric processes do not involve work exchange with the environment. The quantum analogue to volume is, therefore, the energy eigenvalues of the system. Likewise, adiabatic processes have their own valid quantum analogue. Quantum adiabatic processes require that the system be perturbed at a slow enough rate such that no heat is exchanged with the surroundings and, thus, no population excitations occur [46]. Instead, adiabatic processes involve changing the energy eigenvalue while keeping the energy populations constant. To analyze this further, one can consider the internal energy of the system

$$E = \langle \hat{\mathcal{H}} \rangle = \sum_n E_n p_n. \tag{34}$$

The internal energy of the system is the expectation value of its Hamiltonian, which itself is equivalent to the sum of the products of the energy eigenvalues with their respective occupation probability. From Eq. (29), $p_n = e^{-\beta E_n}/Z$ with E having replaced $\hat{\mathcal{H}}$. As was done previously, Eq. (34) is split into work and entropic, i.e., heat, contributions:

$$\mathrm{d}E = \sum_n \left(p_n \mathrm{d}E_n + E_n \mathrm{d}p_n\right) = \mathrm{d}W + \mathrm{d}Q. \tag{35}$$

Therefore, Eq. (35) demonstrates that energy exchange in quantum isochoric processes is entirely entropic, defined by a change in energy populations, $\mathrm{d}p_n \neq 0$, with the energy eigenvalues remaining unchanged, $\mathrm{d}E_n = 0$. On the other hand, adiabatic processes are characterized by work exchange, with changes to the energy eigenvalues, $\mathrm{d}E_n \neq 0$, while the population remains constant, $\mathrm{d}p_n = 0$. Fig. 8(b) illustrates the quantum analogue of the Otto cycle using a QHO to represent the system.

2.3.3 Optomechanically driven quantum heat engine

Having developed the necessary theoretical framework, this section discusses the operating mechanism of the optomechanically driven quantum heat engine. As illustrated in Fig. 9, the device consists of four superconducting CPW resonators. Two operate as heat reservoirs with the resonance frequency of the cold filter resonator, ω_C,

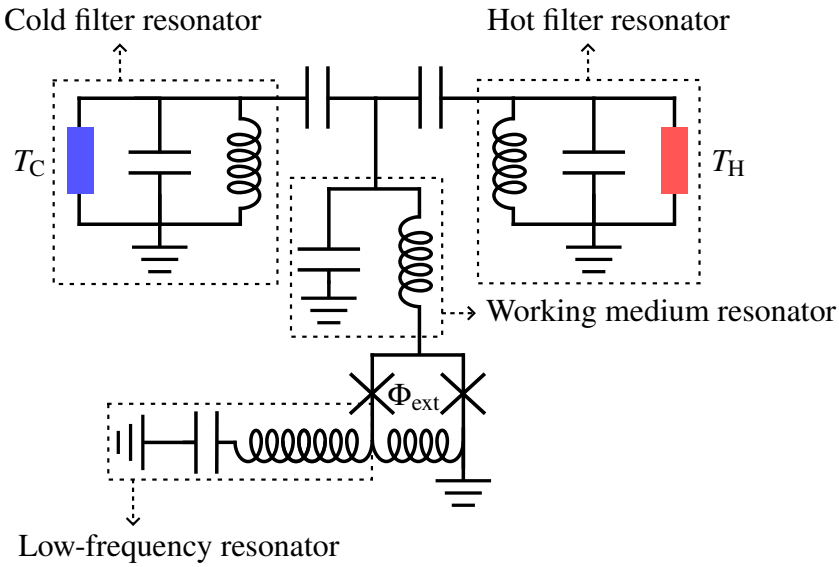

Figure 9: Lumped element circuit model of the AQHE device.

set to be lower than that of the hot filter resonator, ω_H [10]. The resonators achieve this by filtering flat thermal noise from external reservoirs to Lorentzian-shaped power spectra. The Lorentzian-shaped responses of the filters about their resonance frequency is illustrated in Fig. 10(a). Another resonator behaves as the working medium of the heat engine; its resonance frequency, ω_A, is set between the two filter resonators, $\omega_C < \omega_A < \omega_H$, and is modulated such that it periodically couples to and interacts with the hot and cold filter [10]. Fig. 10(b) illustrates the manner by which the resonance frequency of the working medium oscillates between those of the filter resonators. As discussed in Sec. 2.2.1, as the frequency of the working medium approaches that of a filter resonator, its interaction strength with that filter resonator increases. Frequency modulation is mediated by optomechanical-like coupling to the final resonator, whose resonance frequency is set significantly below that of the high-frequency environment consisting of the filter and working medium resonators, $\omega_B \ll \omega_A$ [10]. The low-frequency resonator behaves as a mechanical-like mode and is coupled to the working medium resonator, itself behaving as an optical-like mode, via a SQUID loop [11]. For simplicity, the high-frequency optical-like mode, or working medium, resonator is referred to hereafter as resonator A, and the low-frequency mechanical-like mode resonator is referred to as resonator B. Similar to Fig. 7(b) in Sec. 2.2.2, the SQUID loop is a part of resonator A and is galvanically connected to resonator B. As a result, the signal in resonator B induces a flux that threads the SQUID loop, thereby modulating the resonance frequency of resonator A such that it oscillates between that of the two filter resonators [11]. In Fig. 10b(b), a constant external flux contribution is utilized to adjust the value of ω_A^0. The external flux must therefore be calibrated such that, with the varying flux contribution of resonator B, the behavior in Fig. 10b(b) is achieved.

The optomechanical-like interaction forms the groundwork for the quantum Otto

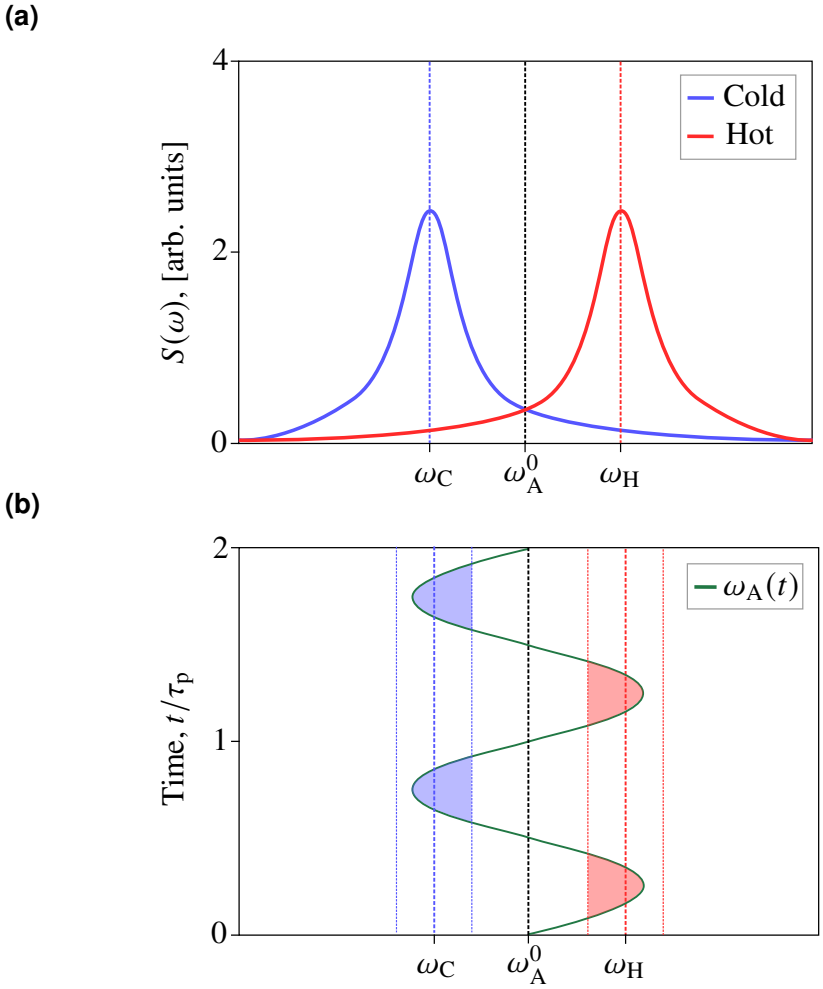

Figure 10: (a) Power spectral density illustration as a function of frequency depicting the Lorentzian response of the hot and cold filter resonators. (b) Time-frequency graph of the frequency of resonator A oscillating, where τ_p is the length of one full oscillatory period, and ω_A^0 is the frequency of resonator A with no flux contribution from the magnetic field of resonator B. The light red and blue shaded sections represent periods of strong interaction between resonator A and, respectively, the hot and cold filter resonators, where its width is determined by the full width at half maximum of the Lorentzian line-shape of the filter resonators.

cycle realized by the device. In the process of pumping photons from the high-temperature to low-temperature filter resonators, energy conservation necessitates an energy boost in resonator B [10]. This boost is realized in the form of excess photons being pumped into the resonator. Aside from an initialization pulse, the device, in theory, requires no further interaction with an external control field; once put into motion, the device cyclically generates work, mediated internally by the SQUID loop [10].

The rate at which and the extent to which power is generated by the device are determined by the quality factor of its components. As [11] theorizes, the amplitude-

dependent dissipation rate in resonator B is derived from its intrinsic dissipation rate and the coherent microwave generation rate. If the total dissipation rate is positive, i.e., the intrinsic dissipation rate is greater than the coherent microwave generation rate, then photons are dissipated faster than they are generated, and thus, the signal amplitude in resonator B dissipates over time. On the other hand, if the total dissipation rate is negative, the amplitude increases in time. The system, eventually, reaches a steady state, wherein photons can, at a constant rate, be extracted from the system for utilization [10]. However, if the quality factor of resonator B is too low, a steady state may not be reached, with the total dissipation rate remaining positive until the signal amplitude reaches zero [11].

3 Methods

This section introduces the measurement setup utilized in experimental runs, which consists of the sample itself, measurement instruments, a dilution fridge, and other components. In addition, the section discusses the algorithms employed to extract measurement data and to perform further analysis.

3.1 Measurement setup

To operate in the quantum regime, as explained in Sec. 2.1.1, the sample is placed in the base mixing chamber of a BlueFors dilution fridge, at a temperature of approximately 25 mK. The device is placed in a sample holder with four ports, each connected to a radio frequency (RF) line. As shown in Fig. 11, the four RF transmission lines are connected to room temperature (RT) via a series of attenuators and amplifiers. The RF lines can be used to probe the low and high-frequency environments of the sample, and to excite the hot filter resonator using high-frequency signals, simulating thermal noise. The input RF lines are attenuated at each temperature stage of the dilution fridge, whereas output lines are amplified using a high-electron mobility transistor (HEMT) amplifier at the 4 K and RT stages. The sample holder is enclosed in a magnetic shield to protect the sample from stray electromagnetic fields, reducing unwanted interference. Inside the magnetic shield, a coil of DC copper wire perpendicularly loops the sample; the magnetic flux generated by the coil threads the SQUID loop, setting a constant external flux value.

From Fig. 11, two measurement setups are possible: probing the low-frequency resonator and probing the high-frequency environment. To probe the low-frequency resonator, a readout signal is sent through the green RF line. The four-port switch, a component capable of switching between two different port orientations ($1 \leftrightarrow 2$ and $3 \leftrightarrow 4$, or $1 \leftrightarrow 3$ and $2 \leftrightarrow 4$), is set to the $1 \leftrightarrow 2$ and $3 \leftrightarrow 4$ configuration. As a result, the cold filter resonator is terminated by a 50 Ω resonator such that it is coupled to the low thermal environment of the base chamber of the dilution fridge. Likewise, a wideband high-frequency signal is sent through the orange RF line to the hot filter resonator; the signal replicates thermal noise and provides a source of non-coherent photons for resonator A, such that the hot filter resonator behaves as a hot bath of photons. To probe the high-frequency environment, the four-port switch is set to the $1 \leftrightarrow 3$ and $2 \leftrightarrow 4$ configuration. RF signal is then sent through the orange transmission line into the hot filter resonator and received out of the cold filter resonator.

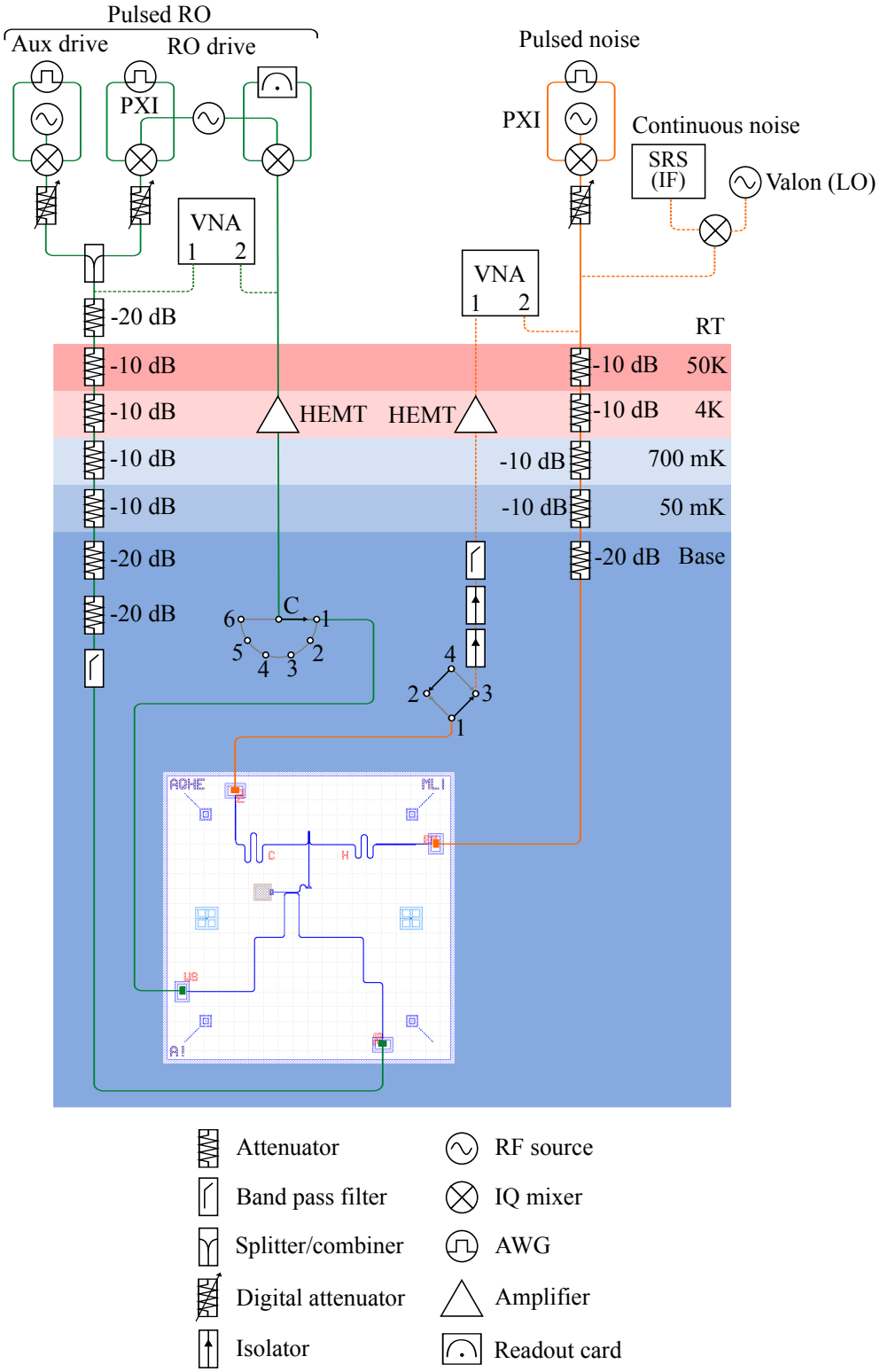

Figure 11: Schematic diagram of the measurement setup at the different temperature stages inside the cryostat alongside a legend for all symbols. The dashed lines indicate interchangeable elements for alternate measurement setups. The names of the devices used for readout and noise signal generation are also given.

Readout (RO) and noise signals can be generated by a range of microwave instruments. A vector network analyzer (VNA) generates a continuous RO signal, the frequency and power of which can be adjusted. From its input and output ports, the VNA is capable of measuring the four scattering parameters, i.e., port 1 $\rightarrow$ 2 transmission (S21), port 1 $\rightarrow$ 1 reflection (S11), port 2 $\rightarrow$ 1 transmission (S12), and port 2 $\rightarrow$ 2 reflection (S22). The VNA performs measurements by continuously sending several RO signals, then returning the average signal magnitude and phase for each frequency in a set range. To sweep across another variable, such as the RO signal power, the process is repeated for different values of said variable. Timed single-shot RO pulses are another option for RO signals; they are generated by an RO drive using a PXI arbitrary waveform generator (AWG), RF sources, and a set of IQ (in-phase—quadrature-phase) mixers. The drives are IQ-mixed, digitally attenuated then combined. The output signal goes through an IQ mixer and is then read by a readout card. Single-shot readout pulses consist of multiple pulses sent through the transmission line. As discussed in Sec. 3.2.2, hundreds of single-shot pulses are averaged to obtain an ensemble average. In addition to frequency and power modulation, the length of the single-shot pulses and the wait-time between them can be adjusted. Timed single-shot pulses can, therefore, be utilized to study the time evolution of the system. Timed single-shot pulses, however, cannot be utilized to probe the high-frequency line; therefore, only continuous RO signals produced by the VNA can be employed on that line.

Similarly, in the experimental setup, noise signals can be generated as either timed pulses or a continuous signal. The continuous signal is generated by up-converting a variable local oscillator (LO) signal produced by a Valon device and a constant intermediate frequency (IF) signal produced by an SRS SG390 device to form a continuous RF signal whose power and central frequency can be varied. Up-conversion is necessary as the SRS noise signal generator, responsible for generating the noise waveform, can only produce frequencies up to 6 GHz [47]. To match the resonance frequency of the hot filter resonator, a central frequency of approximately 10 GHz is required. As a result, the SRS signal must be up-converted with the Valon signal. Section 3.2.1 discusses the mechanism by which microwave mixing occurs to produce an up-converted output signal at an adjustable frequency. Therefore, at this point, it is sufficient to only note that the output RF signal has a Gaussian-like power spectral density, which is designed to peak near the resonance frequency of the hot filter resonator. On the other hand, the power spectral density of timed noise pulses can be made more flat around a chosen central frequency. The timed pulses are produced using a noise drive generated by a PXI AWG, and their central frequency, power, length, and wait time can be adjusted. Using carefully chosen wait times between pulses, it is also possible to transform the timed pulses into a near continuous signal. As true thermal white noise is continuous with a flat power spectral density, this has the benefit of more accurately replicating thermal noise. Fig. 12 visualizes the continuous and single-shot readout signals, and the continuous and pulsed noise signals. For the single-shot readout pulses, Fig. 12 illustrates two single-shot pulses of equal length and the wait time between them. Each pulse is averaged according to the mechanism described in Sec. 3.2.2. In practice, hundreds of these pulses are sent, and

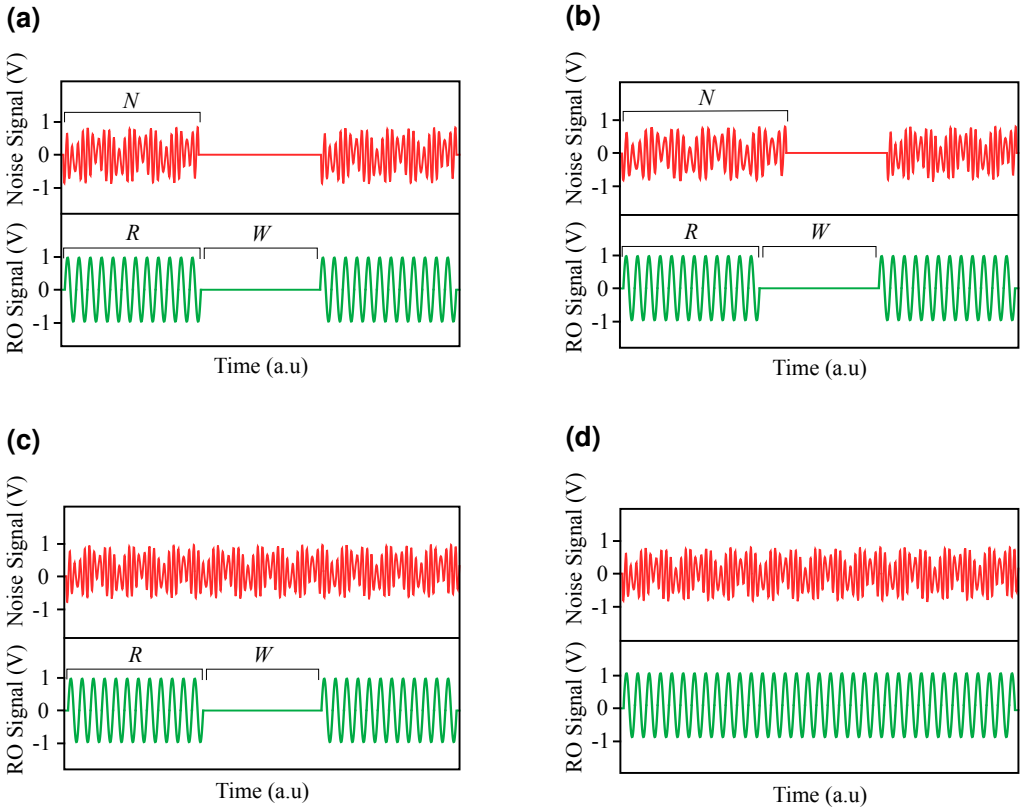

Figure 12: Schematic illustration of the noise and readout signal waveforms in different configurations, where N is the noise pulse length, R is the single-shot readout pulse length, and W is the wait time between single-shot readout pulses. The voltage values are arbitrary and do not reflect actual measurement values. (a) Pulsed readout (PXI) and noise (PXI) signal of equal length (b). Pulsed readout (PXI) and noise (PXI) signal of different length. (c) Continuous noise (Valon) signal and pulsed readout (PXI) signal. (d) Continuous noise (Valon) signal and continuous readout (VNA) signal.

an ensemble average is calculated from the average of each single-shot pulse.

3.2 Modulation and Characterization

To perform characterization measurements on the sample, the amplitude and phase of the transmitted RO signal are analyzed while modulating different variables, such as the noise power. This section, therefore, explains the mechanism by which LO and IF signals are mixed to produce RF noise signals. Furthermore, this section also discusses RO signal generation alongside amplitude and phase extraction, i.e., I-Q mixing. Finally, a brief description of the circle fit technique for scattering data analysis is given.

3.2.1 Microwave mixing

Microwave mixing generally involves mixing two incoming signals to produce a single output signal whose frequency is a translation of the two input signals [48]. A mixer is a multi-port device that facilitates the mixing process, and it consists of RF, IF, and LO ports. It is generally represented with the circuit symbol depicted in Fig. 13. The LO port behaves as the control gate and is always an input port. Mixing occurs when the LO signal is at a sufficiently large voltage, whereas it stops when the LO signal voltage is too low [48]. On the other hand, the RF and IF ports can be interchangeably used as input and output ports; the behavior of the microwave mixer depends on this choice. Down-conversion occurs when the RF port is chosen as the second input port. As a result, the frequency of the output IF signal is lower than the input RF frequency by the following formula, $f_{\mathrm{IF}} = |f_{\mathrm{LO}} - f_{\mathrm{RF}}|$ [48].. In contrast, if it is desired that the frequency of the output signal is larger than that of the input signal, up-conversion is required. Up-conversion involves using the IF port as the second input and the RF port as the output. The frequency of the resulting output signal is larger than that of the input IF signal as follows, $f_{\mathrm{RF}} = f_{\mathrm{LO}} \pm f_{\mathrm{IF}}$ [48]. Generally, up-conversion results in two output RF signal peaks at different frequencies. Both RF signal peaks occur at frequencies above that of the IF signal, with one peak appearing below the LO signal frequency and the other appearing above the LO signal frequency. This type of up-conversion is called double-sided conversion [48]. While certain microwave mixers are capable of single-sideband conversion, i.e., where only one RF signal peak appears, the mixer used in this work employs double-sided conversion. Fig. 14 illustrates the two forms of conversion on a spectral power density diagram.

3.2.2 IQ mixing and extraction

An IQ mixer is a device used to extract the amplitude and phase value of an output RO signal [26]. Inversely, it can be used to create an RO signal with specific values for amplitude and phase [49]. This section, however, focuses only on the former application while the latter is omitted as it is the inverse process (i.e., digital to analog

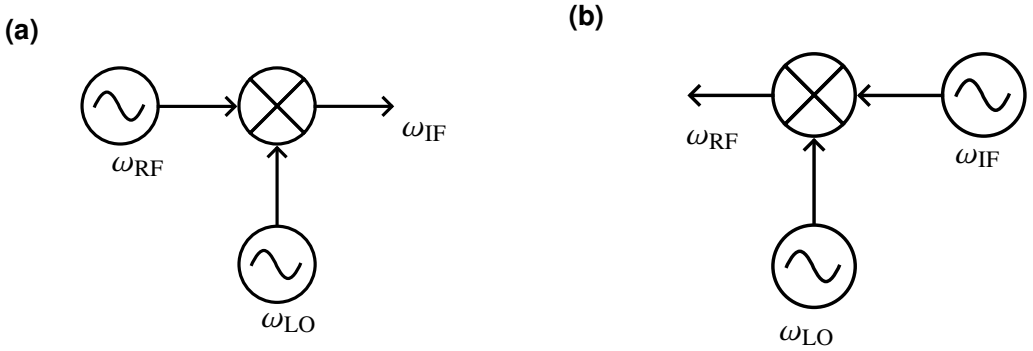

Figure 13: (a) Schematic representation of (a) downconversion and (b) upconversion using the mixer circuit component.

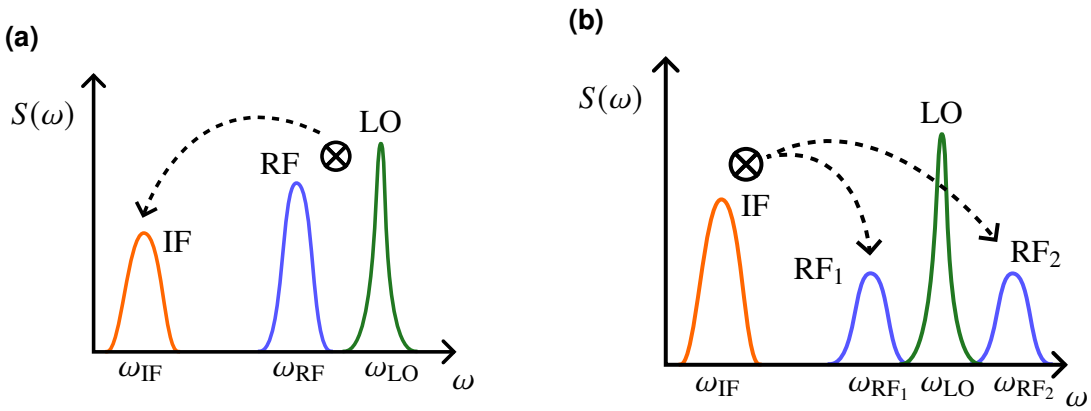

Figure 14: Power spectral density graph as a function of frequency illustrating (a) downconversion and (b) double-banded upconversion.

$\leftrightarrow$ analog to digital). After probing the device, an RO signal is of the following form

$$s(t) = A_{\mathrm{RO}} \cos\left(\omega_{\mathrm{RO}} t + \theta_{\mathrm{RO}}\right), \tag{36}$$

where ω_{RO} is the frequency of the RO signal, A_{RO} is its amplitude, and θ_{RO} is its phase [26]. Eq. 36 can be written using the phasor form discussed in Sec. 2.1.2

$$s(t) = \Re\{A_{\mathrm{RO}} e^{\mathrm{i}(\omega_{\mathrm{RO}} t + \theta_{\mathrm{RO}})}\} = \Re\{A_{\mathrm{RO}} e^{\mathrm{i}\theta_{\mathrm{RO}}} e^{\mathrm{i}\omega_{\mathrm{RO}} t}\}. \tag{37}$$

As ω_{RO} is a known quantity, i.e., the frequency used to probe the device, the phasor $A_{\mathrm{RO}} e^{\mathrm{i}\theta_{\mathrm{RO}}}$ in Eq. 37 contains all the information needed to study the behavior of the device. This phasor is split into an in-phase component, I, and a quadrature component, Q

$$A_{\mathrm{RO}} e^{\mathrm{i}\theta_{\mathrm{RO}}} = A_{\mathrm{RO}} \cos\theta_{\mathrm{RO}} + \mathrm{i} A_{\mathrm{RO}} \sin\theta_{\mathrm{RO}} \equiv I + \mathrm{i}Q. \tag{38}$$

From Eq. 38, amplitude and phase can be defined in terms of I and Q as follows

$$A_{\mathrm{RO}} = \sqrt{I^2 + Q^2}, \tag{39}$$

$$\theta_{\mathrm{RO}} = \arctan\left(Q/I\right). \tag{40}$$

As depicted in Fig. 15, the IQ mixing process involves splitting the incoming RO signal $s(t)$ into two signals, with each equal to $s(t)/2$. The signals are then mixed with an LO signal $y_{\mathrm{LO}}(t) = (A_{\mathrm{LO}}/2)\cos(\omega_{\mathrm{LO}} t)$ for down-conversion such that their frequency becomes $\omega_{\mathrm{IF}} = |\omega_{\mathrm{RO}} - \omega_{\mathrm{LO}}|$. The LO frequency, ω_{LO}, is chosen such that $\omega_{\mathrm{IF}} = 0$ (i.e., homodyne modulation) or $\omega_{\mathrm{IF}} > 0$ (i.e., heterodyne modulation) [26]. The I branch is mixed with the unchanged LO signal $y_{\mathrm{I}}(t) = y_{\mathrm{LO}}(t)$ while the Q branch is mixed with the $\pi/2$ shifted LO signal $y_{\mathrm{Q}}(t) = -(A_{\mathrm{LO}}/2)\sin(\omega_{\mathrm{LO}} t)$. After mixing, the signals in the I and Q branches are represented as $I(t)$ and $Q(t)$, respectively, and are $\pi/2$ out of phase with one another. To extract values for I and Q, the signals are

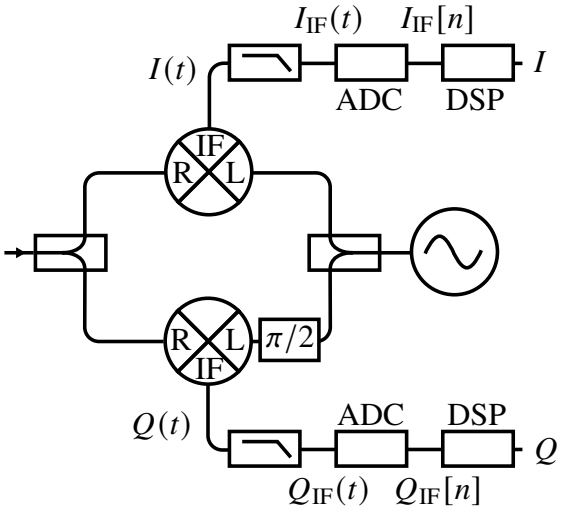

Figure 15: Schematic diagram of the IQ extraction process using an RF source, two microwave mixers, a low band-pass filter, an analog-to-digital converter (ADC), and a digital signal processor (DSP). The output after each stage is given in italics.

first low-pass filtered (i.e., time-averaged):

$$I_{\mathrm{IF}}(t) = \frac{1}{T}\int_0^T \frac{s(t)}{2} y_{\mathrm{I}}(t)\,\mathrm{d}t = \frac{A_{\mathrm{RO}}A_{\mathrm{LO}}}{8}\cos\left(\omega_{\mathrm{IF}}t + \theta_{\mathrm{RO}}\right), \tag{41}$$

$$Q_{\mathrm{IF}}(t) = \frac{1}{T}\int_0^T \frac{s(t)}{2} y_{\mathrm{Q}}(t)\,\mathrm{d}t = \frac{A_{\mathrm{RO}}A_{\mathrm{LO}}}{8}\sin\left(\omega_{\mathrm{IF}}t + \theta_{\mathrm{RO}}\right). \tag{42}$$

After low-pass filtering, the frequency is low enough such that digital demodulation using an analog-to-digital converter (ADC) can proceed [26]. The digital signals are written as:

$$I_{\mathrm{IF}}[n] = \frac{A_{\mathrm{RO}}A_{\mathrm{LO}}}{8}\cos\left(\Omega_{\mathrm{IF}}n + \theta_{\mathrm{RO}}\right), \tag{43}$$

$$Q_{\mathrm{IF}}[n] = \frac{A_{\mathrm{RO}}A_{\mathrm{LO}}}{8}\sin\left(\Omega_{\mathrm{IF}}n + \theta_{\mathrm{RO}}\right), \tag{44}$$

where $n = t/\Delta t$ is the index of the sample number, Δt is the sampling time, and $\Omega_{\mathrm{RO}} = \omega_{\mathrm{IF}}t$ is the digital frequency. Generally, sampling begins after a certain wait time τ_{wt}. Both the sampling period and wait time are illustrated in Fig. 16(a). Each sample point can then be represented on the complex IQ plane as follows:

$$z_{\mathrm{IF}}[n] = I_{\mathrm{IF}}[n] + \mathrm{i}Q_{\mathrm{IF}}[n] = \frac{A_{\mathrm{RO}}A_{\mathrm{LO}}}{8} e^{\mathrm{i}\theta_{\mathrm{RO}}} e^{\mathrm{i}\Omega_{\mathrm{IF}}n} \tag{45}$$

To digitally demodulate the sample points, each point in the vector z_{IF} is multiplied by the complex conjugate of its respective oscillating component:

$$z[n] = z_{\mathrm{IF}}[n] \times e^{-\mathrm{i}\Omega_{\mathrm{IF}}n}. \tag{46}$$

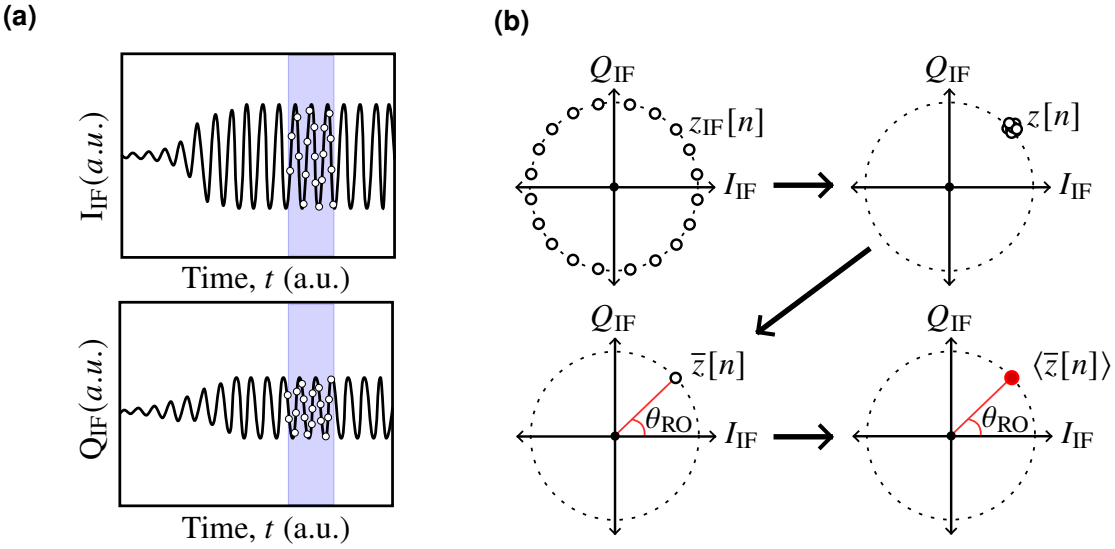

Figure 16: (a) Diagram of the analog to digital conversion of the I_{IF} and Q_{IF} signal. The white dots depict the sample points $I_{IF}[n]$ and $Q_{IF}[n]$, and the light blue strip represents the sample time after some initial wait time. (b) Schematic of the digital signal process. First, the oscillating component of the sample points is removed. Then, the points are averaged to a single point in the IQ plane $\overline{z}[n]$. This process is repeated several times to attain an ensemble average $\langle\overline{z}[n]\rangle$. The angle of the final point with respect to the I plane is θ_{RO} while its amplitude is proportional to A_{RO}.

The average of these points is taken as the "single-shot" result:

$$\overline{z}[n] = \frac{1}{N}\sum z[n] = \frac{A_{RO}A_{LO}}{8}e^{i\theta_{RO}}, \tag{47}$$

where N is the total number of sample points. This process can be repeated several times, as discussed in 3.1, to produce an ensemble average $\langle\overline{z}[n]\rangle$. In both the ensemble and single-shot approach, the position of the final point on the plane yields values for I and Q, from which amplitude and phase are calculated according to Eq. 39 and 40. Sec. 4.3 utilizes the ensemble approach for time domain measurements by adjusting the wait time between the single-shot pulses.

3.2.3 Scattering data analysis

As introduced in Sec. 2.1.2 and Sec. 2.1.3, an LC resonator is characterized primarily by its resonance frequency and quality factor. The loaded quality factor Q_l is split into the internal and external quality factors, Q_{int} and Q_{ext}. It is possible to determine the quality factor of a resonator by using scattering data analysis on transmission measurements. To extract the quality factor of the resonator from these measurements, this thesis employs the algorithm described in [12]. The algorithm begins by performing a high-resolution transmission sweep of the resonator to extract several S_{21} values across a range of frequencies. The frequency points should be sufficient and distributed

evenly across the frequency span, which, ideally, should be four times the linewidth of the resonator [12].

Uncalibrated data is first calibrated to remove circular distortions by accounting for and removing cable delay [12]. Calibrated data is then algebraically fit to a circle centered at (x_c, y_c) with radius r_0 in the $\Re(S_{21})$ and $\Im(S_{21})$ plane. Subsequently, the impedance mismatch ϕ_0 is calculated using $\phi_0 = -\arcsin(y_c/r_0)$ [12]. A translation operation is then carried out to shift the fitted circle to the origin of the $\Re(S_{21})$ and $\Im(S_{21})$ plane. To then calculate the loaded quality factor Q_l and resonance frequency f_r, an initial value for offset phase is calculated using $\theta_0 = (\phi_0 + \pi) \bmod \pi$ [12]. Q_l and f_r can then be determined using

$$\theta(f) = \theta_0 + 2\arctan\left(2Q_l r_0\left[1 - \frac{f}{f_r}\right]\right), \tag{48}$$

where $\theta(f)$ is the phase fit derived from the calibrated and translated circle for a given frequency [12]. Finally, the complex external quality factor Q_{ext} is calculated as $Q_{ext} = Q_l/\left(2r_0 e^{-i\phi_0}\right)$ [12]. Accordingly, the internal quality factor Q_{int} is derived using $Q_{int}^{-1} = Q_l^{-1} - \Re\{Q_{ext}^{-1}\}$.

4 Results and discussion

This section presents measurement results from several experimental runs and deduces the properties and behaviors of the low-frequency resonator. While it is possible to probe both the high and low-frequency environments of the device, issues with the four-port switch and the high-frequency HEMT amplifier rendered it difficult to extract tangible measurement results. Thus, the results presented in this work are entirely of the low-frequency regime. As the low-frequency resonator is responsible for storing the usable work output of the device, its results are sufficient to analyze the extent to which energy is generated and stored. The measured resonance frequency of the low-frequency resonator at the zero-flux point is 317.25 MHz, while those of the hot and cold filter resonators are respectively 10.300 GHz and 9.037 GHz from previous measurements. Finally, the working medium resonator has a measured resonance frequency of 11.255 GHz when the external flux through the SQUID loop is 0.

4.1 Preliminary calibration

Before performing characterization measurements, it is necessary to investigate the effect that adjusting certain variables has on the device. As explained in Sec. 3.1, the measurement setup has a significant amount of degrees of freedom. Thus, preliminary calibration runs are required to find ideal values for each degree of freedom. It is important to note that ideal values fluctuate based on the combination of readout and noise signal used alongside the thermal environment of the cryostat. Therefore, this section introduces a generalizable calibration process whose results may not be reflected throughout the text, given that different ideal values appear depending on the specific measurement conditions. Nevertheless, when the measurement conditions do change, the same calibration process is repeated to attain updated ideal values.

As discussed in Sec. 2.3.3, the combination of the constant external flux with the modulating flux from the low-frequency resonator produces a combined modulating flux that threads the SQUID loop. In Fig. 10(b), changing the external flux varies the position of the central frequency ω_{A}^{0} while the low-frequency resonator flux is primarily responsible for the modulation depicted by the green line $\omega_{\mathrm{A}}(t)$. Therefore, determining an ideal value for external flux is necessary for achieving the process described in Fig. 10(b). The constant external flux is produced by a magnetic coil connected to a voltage source at room temperature. The voltage from this source is adjusted to modulate the flux threading the SQUID loop produced by the coil. Based on this, voltage sweeps are carried out to find the ideal flux value, which is also referred to as the flux sweet spot.

Fig. 17 displays two spectroscopies with flux sweeps. Fig. 17(a) was measured using a continuous readout signal and no noise signal, whereas Fig. 17(b) was measured with a continuous readout signal and an optimized near-continuous noise signal. The optimized near continuous noise signal is described in Sec. 3.1 and involves adjusting the wait time of the noise pulses such that they are effectively continuous. As a result, the sweep employs a readout and noise signal combination similar to that depicted in Fig. 12(d). In Fig. 17(a), it is clear that adjusting the flux voltage results

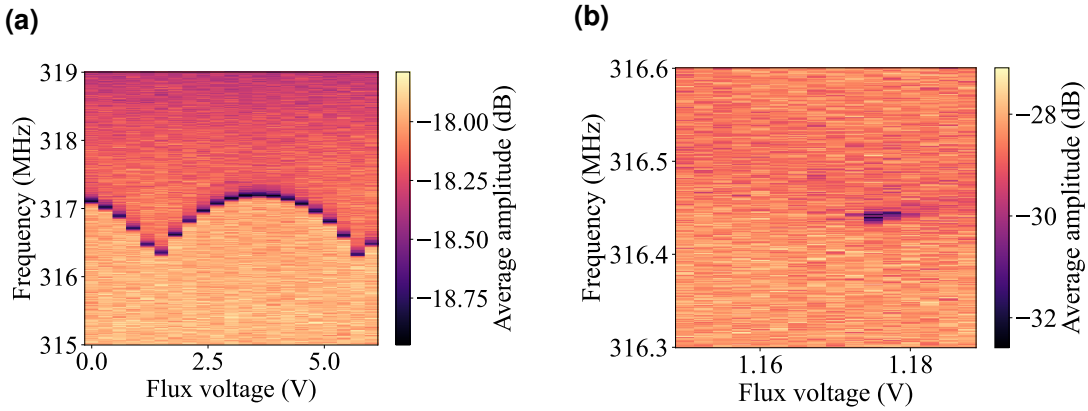

Figure 17: (a) Average readout amplitude as a function of flux voltage and readout signal frequency. Measurement was carried out with a continuous readout signal (VNA) at −25 dB power without a noise signal. (b) Focused flux voltage sweep around the flux sweet spot, marked by the greater amplitude dip. Measurement was carried out with a continuous readout signal (VNA) at −30 dB and an optimized near-continuous noise signal (PXI) with 18 dB of attenuation.

in periodic oscillation of the resonance frequency of the low-frequency resonator. The resonance frequency is marked by dips in the average readout signal amplitude, which, as discussed, occurs due to energy exchange with the resonator. The oscillatory period is approximately 4.5 V with the resonance frequencies ranging from 316.4 MHz to 317.25 MHz. Since the SQUID loop is coupled to the low-frequency resonator, adjusting the magnetic flux through the SQUID loop also modulates its resonance frequency, which explains the results found in Fig. 17(a). However, since the SQUID loop terminates the working medium resonator and is, therefore, primarily coupled to it, adjusting flux voltage has a more significant effect on its resonance frequency compared to the low-frequency resonator. As a result, the resonance frequency of the low-frequency resonator only oscillates by 0.85 MHz, whereas the frequency of the working medium resonator oscillates by approximately 1 GHz throughout the heat engine cycle based on the designed resonance frequencies of the hot and cold filter resonators.

In Fig. 17(b), a noise signal is sent to act as an effective thermal reservoir through the hot filter resonator such that the heat engine cycle can run. The figure displays a focused voltage sweep between 1.150 V and 1.1875 V, which was carried out to find the most accurate voltage value for the flux sweet spot. It was found that an enhanced resonance dip occurs between 1.170 and 1.180 V at 316.445 MHz. While some measurements in the thesis were carried out immediately after this result with a flux voltage value of 1.173 V, others were carried out at different times or with different measurement setups. Given that the flux sweet spot is susceptible to changes based on the magnetic and thermal environment of the cryostat, the flux voltage sweet spot is not constant for all measurements in this thesis. Nevertheless, the flux sweet spot always appears as it indicates the point at which optimal detunings between the

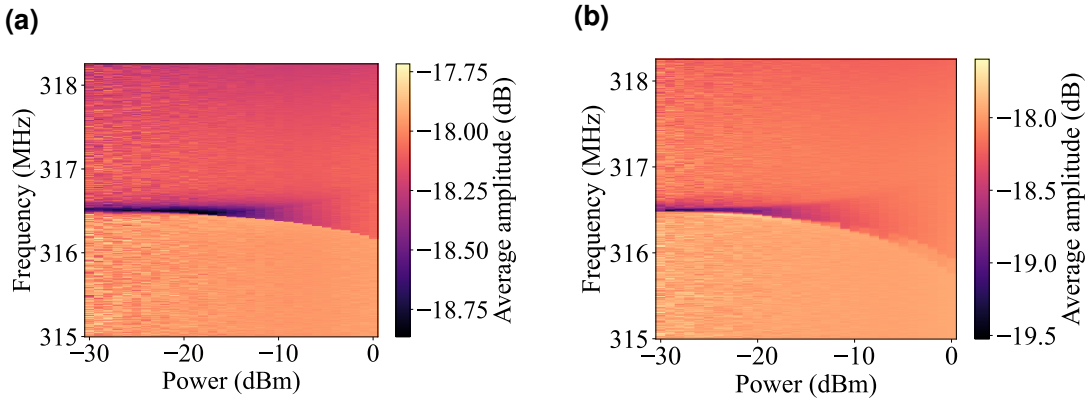

Figure 18: Continuous readout signal (VNA) power sweeps at different continuous noise (Valon) powers. (a) No noise signal. (b) -16 dB noise signal.

working medium and the filtering resonators are acquired.

In addition to external flux, the power of the readout signal sent through the low-frequency transmission line in Fig 11 can also be varied. Fig. 18 displays two readout signal power sweeps between the values −30 and 0 dB. One is carried out with no noise signal, and the other with the continuous noise signal (Valon) set at its ideal value. In the measurement runs, a continuous readout signal is employed. Based on the measurements, it is observed that a sharp resonance dip appears between −30 and −20 dB in both cases. However, in the run with the noise signal, the resonance dip is enhanced by approximately 1 dB at a readout power of −29 dBm. At larger readout powers, the resonance dip widens due to nonlinearities in the system. These nonlinearities emerge from the SQUID coupling of the working medium and low-frequency resonators. When a resonator is coupled to a combined resonator-SQUID subsystem, as is the case for the low-frequency resonator, large readout signal powers result in a 'punch-out' [13]. The 'punch-out' causes the resonator to default to its bare frequency, eliminating the Lamb shift [13]. Without a noise signal, the 'punch-out' begins around −15 dB. However, with the noise signal, the 'punch-out' begins at lower readout powers, with it appearing around −20 dB.

The noise signal power is the last major degree of freedom that can be adjusted. This variable determines the strength of the noise signal utilized to generate the hot reservoir through the hot filter resonator, with a more powerful signal effectively corresponding to a higher temperature reservoir. Fig. 19 displays the effect that varying noise signal power has on the device for different noise signal configurations. Fig. 19(a) involves utilizing the continuous noise signal (Valon) configuration, whereas Fig. 19(b) utilizes the optimized near-continuous noise signal (PXI) configuration. For the continuous noise signal (Valon), the noise power can be directly adjusted, whereas digital attenuators are employed to vary the power of the optimized near-continuous noise signal. In Fig. 19(a), enhanced resonance occurs between −17.5 and −13 dBm. Between these values, the resonance dip is enhanced by approximately 1.5 dB compared to the bare resonance dip observed at low noise powers. At larger

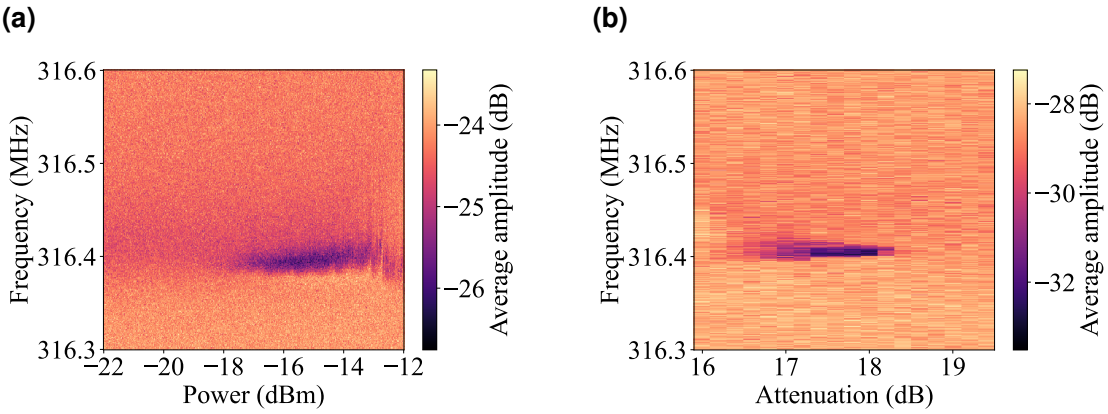

Figure 19: Noise power sweeps for different noise signal types. (a) Continuous noise signal (Valon). (b) Optimized near-continuous noise signal (PXI).

noise powers, the resonance dip widens, and a reduction in enhancement is observed. Similar behavior is observed in Fig. 19(b). For reduced signal attenuation, which corresponds to a stronger noise signal, the resonance dip widens and is no longer enhanced. Between 17 and 18 dB, the resonance dip is enhanced by roughly 4 dB, with the most significant enhancement occurring at 17.65 dB of attenuation. With greater attenuation, the system responds similarly to the low power case in Fig. 19(a), with the enhancement weakening.

4.2 Enhanced resonance

Upon calibrating the measurement setup, an enhanced resonance dip was observed with the noise signal. To easily discern the enhanced resonance dip, simple frequency sweeps were carried out such that the results are represented as a line rather than a color map.

Fig. 20(a) displays the averaged readout signal amplitude in dB plotted against the readout signal frequency in MHz for noise signal on and off. A line fit connects the individual scatter points. Both the readout and noise signal were continuous. The readout signal power was set to −27 dB, and the noise signal power was set to −18.5 dB with the external flux set to 1.173 V following the same calibration process described in Sec. 4.1. The orange line represents the results with the noise signal off, while the purple line represents the results with the noise signal on. Results with the noise signal display an enhanced resonance dip compared to those without the noise signal. The resonance dip is enhanced by roughly 4 dB when the noise signal is turned on.

Repeating the same measurement process with a different noise signal source, a similar enhanced resonance dip is observed. In Fig. 20(b), the optimized near continuous noise signal is employed instead of the continuous noise signal utilized in Fig. 20(a). The readout signal power is set to −30 dB with the near continuous noise signal digitally attenuated by a value of 17.65 dB, with the flux set to 1.173 V in

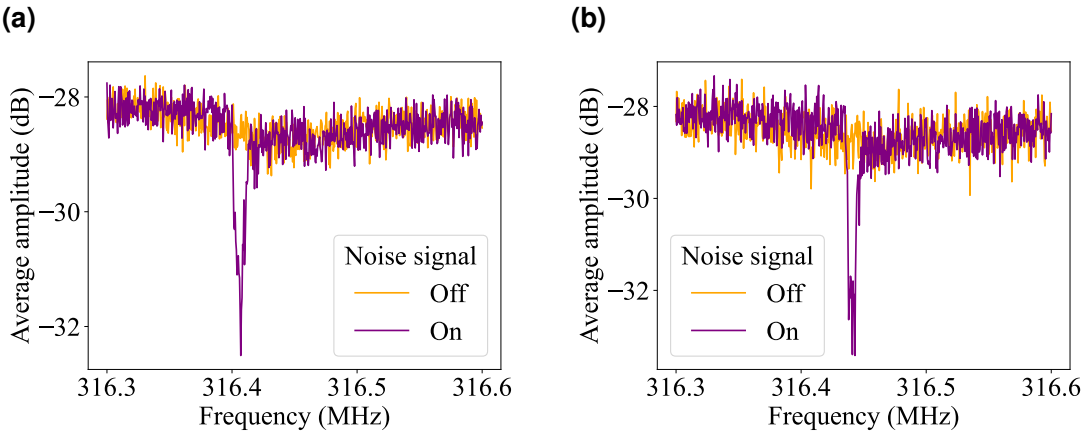

Figure 20: Averaged transmitted amplitude of the continuous readout signal (VNA) as a function of the readout signal frequency with and without the (a) continuous (Valon) noise signal set at −25 dB power. (b) near continuous (PXI) noise signal with 17.65 dB attenuation.

line with the calibration process. As is observed, the resonance dip is significantly enhanced by approximately 4.5 dB when the noise signal is turned on compared to when it is turned off. The resonance frequency in Fig. 20(b) is shifted from its value in Fig. 20(a) by approximately 0.4 MHz. This may be a result of differences between the two noise signal configurations or a result of changes in the measurement environment, e.g., the temperature of the base mixing chamber.

4.3 Time domain analysis

While the results in Sec. 4.2 prove that energy generation does occur in the system, with photons being pumped into the low-frequency resonator, the extent to which energy storage occurs must also be considered. To measure the evolution of the system, time domain measurements are carried out by utilizing the timed readout pulses described in Sec. 3.1.

To analyze the base evolution of the low-frequency resonator, the readout and noise signal configuration depicted in Fig. 12(a) is utilized. This is done in Fig. 21 where the readout and noise pulse length are equal and kept constant while the wait time between single readout shots is swept. The purpose of this run is to analyze energy storage in the low-frequency resonator when the heat engine cycle is turned off for different lengths of time. An enhanced resonance dip appears near the resonance frequency of the low-frequency resonator, centered around 316.45 MHz. However, the enhanced resonance dip weakens, returning to the bare resonance case for measurements with a wait time greater than 6 µs. Although the weakening of the resonance dip with longer wait times is expected due to the lifetime of the resonator, given that the noise signal is turned off during the wait time, the rate at which it occurs is greater than is desired. This suggests that the low-frequency resonator is rapidly relaxing to the

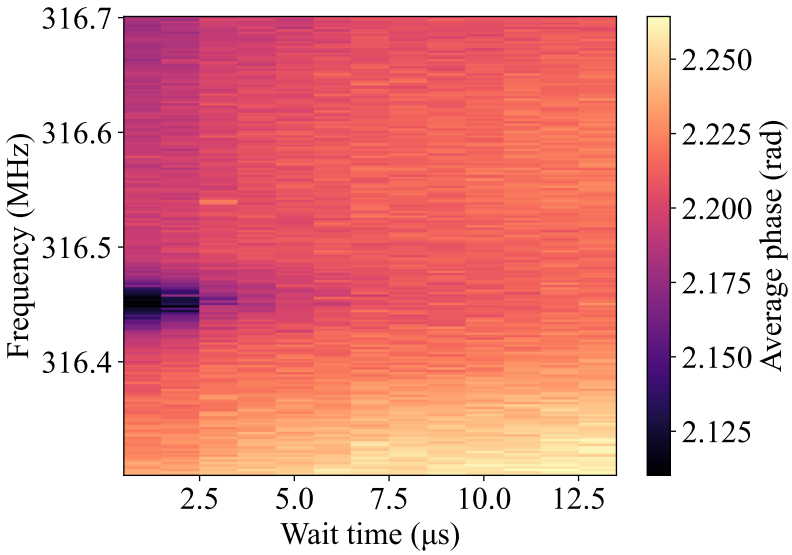

Figure 21: Wait time sweep as a function of readout signal (PXI) frequency. A pulsed noise signal (PXI) is employed with a length equal to that of the readout pulse.

ground state following the short bursts of energy generation, i.e., pulses of readout and noise signal. Therefore, this result is not ideal as it indicates that the dissipation rate of the low-frequency resonator, i.e., the rate at which energy decays from the resonator, is large. The dissipation rate of the resonator is primarily linked to the fabrication process of the resonator, and it can generally be enhanced by minimizing defects in the different resonator components. Nevertheless, if the dissipation rate is above a certain threshold, the low-frequency resonator dissipates energy faster than it receives it from other parts of the system. As a result, coherent energy generation in time may not occur with the low-frequency resonator decaying faster to the ground state.

To further investigate the aforementioned issue and conclusively determine whether the dissipation rate is greater than the photon generation rate, the signal configuration depicted in Fig. 12(c) is employed, i.e., the readout signal is sent as timed pulses whereas the noise signal is near-continuous. As a result, during the readout wait time, the noise signal continues to excite the hot filter resonator, which maintains the heat engine cycle and results in continuous energy generation. In a system with minimal dissipation, longer wait times result in, to an extent, greater readout resonance dips as the system has more time to generate energy. However, if the dissipation rate of the low-frequency resonator is greater than the rate at which energy is pumped into the resonator, the opposite is true. In that case, longer wait times between readout pulses result in shallower readout resonance dips as the resonator has more time to relax to the ground state. To determine which of these regimes the low-frequency resonator is operating in, the measurement runs shown in Fig. 22 were carried out.

Fig. 22 displays the averaged amplitude and phase of two experimental runs. As can be ascertained from both the amplitude and phase diagram, an enhanced resonance dip appears only in the 2 μs case. On the other hand, in the 20 μs case, an enhanced resonance dip does not appear, with the results appearing similar to

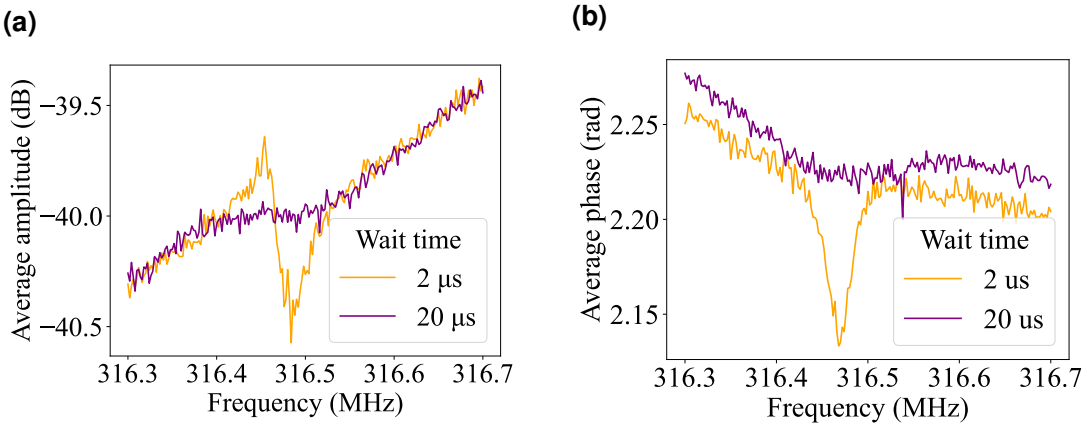

Figure 22: (a) Averaged pulsed readout signal (PXI) amplitude as a function of the readout signal frequency. The pulsed readout signal is of amplitude 1 V and set to a length of 6 microseconds. Pulsed noise (PXI) of amplitude 5 V is utilized, with the noise pulse length set as the sum of the readout pulse length and wait time between subsequent readout pulses. The wait time is set to 2 microseconds in one run and 20 microseconds in another. (b) Averaged pulsed readout signal (PXI) phase as a function of the readout signal frequency. The setup and parameters are the same as in (a).

frequency spectroscopy measurements with no noise signal. Comparing the results to the two cases introduced previously, it can be concluded that the low-frequency resonator operates in the case where the dissipation rate is greater than the rate at which energy is pumped into the resonator.

4.4 Quality factor analysis

The observed properties in Sec. 4.3 are further investigated by analyzing the quality factor of the resonator. As aforementioned, the quality factor is the ratio of energy stored to energy dissipated in a single cycle. To perform the analysis, the algorithm described by [12] is utilized via a Python package.

By applying the algorithm to the noise power sweep presented in Fig. 19(a), the results shown in Fig. 23 are attained. The sweep involved a -30 dB continuous readout signal in order to minimize the photon number in the resonator. Fig. 23(a) displays the external and internal quality factors of the low-frequency resonator. The external quality factor first increases at -18 dB to 2×10^5 at -17 dB before gradually decreasing to 10^5 at -12 dB. Comparatively, the internal quality factor is lower, increasing at -18 dB to 2.1×10^4 at -16 dB, then decreasing down to 8×10^3 at -12 dB. The internal quality factor is within the expected range for the tadpole-type resonator utilized in the device [50].

In addition to individually analyzing the internal and external quality factor contributions, it is possible to analyze the total, or loaded, quality factor of the resonator with the same package. Furthermore, by treating the thermal noise signal

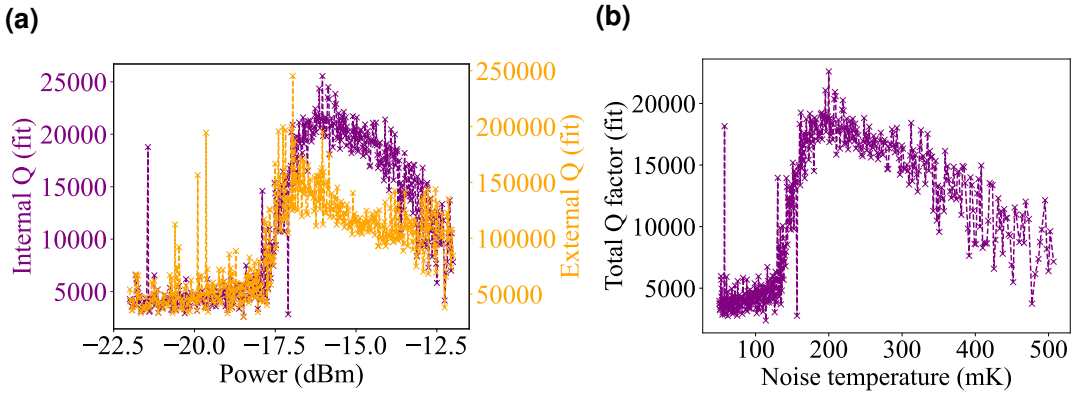

Figure 23: (a) Internal and external quality factor of the low-frequency resonator as a function of the noise signal power. (b) Total quality factor as a function of noise temperature according to the output power of Johnson-Nyquist noise.

as Johnson-Nyquist noise, values for noise temperature can be derived from the noise signal power and the attenuation chain. Using the internal and external quality factors in Fig. 23(a), Fig. 23(b) displays the loaded quality factor as a function of noise temperature. The loaded quality factor hovers between 2.5×10^3 and 5×10^3 until the noise temperature reaches 100 mK. At that temperature, the loaded quality factor increases sharply up to 1.8×10^4 around 200 mK. The increase occurs due to increased excitations of the hot filter resonator at higher noise temperatures, which may contribute to increased photon generation in the system. A quality factor of 1.8×10^4 is below the theoretical values required for autonomous heat engine operation. Larger quality factors are necessary for the resonator to operate with a negative dissipation rate. Otherwise, the intrinsic dissipation rate of the resonator exceeds the energy generation rate of the system [11].

5 Conclusions

This thesis experimentally studied the low-frequency, energy-storing resonator in a proposed autonomous quantum heat engine. The work first established the theoretical background relevant to the device. The circuit QED elements utilized in the device were introduced, and their interaction with one another was also discussed. Then, the optomechanical-like coupling of superconducting resonators was studied, establishing a framework for the autonomous operation of the heat engine. To conclude the theoretical section, principles of quantum thermodynamics were introduced alongside the quantum analog to the Otto cycle. Accordingly, the individual elements of the theoretical section were contextualized by presenting the operating mechanism of the autonomous quantum heat engine.

Following the theoretical segment, the methods employed to experimentally analyze the resonator were introduced. The section presented the setup of the device in the cryostat alongside the measurement equipment utilized to probe the resonator. In addition, the different readout and noise signal configurations were presented and visualized. The transmission line measurement process was further discussed by presenting the microwave mixing, digital demodulation, and data analysis processes, with each representing signal generation, processing, and post-processing. Accordingly, the algorithm employed to extract the quality factor from the probe measurements was also presented.

Before characterization, calibration measurements were performed to find ideal values for the different degrees of freedom in the system. Sweeps of external flux voltage, noise signal power, and readout signal power were carried out. From these sweeps, values corresponding to an enhanced resonance dip were noted for utilization in later runs. While the ideal values vary for different signal configurations and measurement conditions, and thus, change throughout the work, this section presented the common calibration process by which these values were determined.

The work first analyzed changes to the resonance dip of the low-frequency resonator when a noise signal is introduced to the hot filter resonator. This was carried out by comparing spectroscopy results with and without the noise signal. To completely evaluate the behavior of the resonator, measurements were carried out with two noise signal types: continuous noise with a Gaussian spectral density and near-continuous noise with a flat spectral density. For both noise configurations, a similarly valued, significant enhancement in the resonance dip was observed when compared to the bare, no-noise case. While these results do not conclusively prove that the heat engine operates as previously theorized, they reveal that the energy in the low-frequency resonator increases when a noise signal is sent into the hot filter resonator. Utilizing averaged single-shot readout pulses, a time domain analysis of the resonator was also completed. A sweep of the wait time between single-shot readout pulses was first carried out. The results reveal that the lifetime of the resonator is short, suggesting that the intrinsic dissipation rate of the resonator is large. In another measurement run, the noise signal was kept on during the wait time. As the wait time increased, the resonance dip was no longer enhanced, appearing instead as a noise-free frequency spectroscopy result. This run indicates that the intrinsic dissipation rate of the resonator

is larger than the rate at which energy is pumped into the resonator. To conclude the results section, the quality factor of the resonator was found. Referring to noise signal power sweeps, the quality factors as a function of noise power and temperature were extracted. While the internal quality factor was within the acceptable range for the type of low-frequency resonator, the loaded quality factor was below the theoretical threshold for autonomous operation of the heat engine.

Moving forward, similar characterization measurements of the high-frequency environment must be performed in order to develop a complete description of the device. This work was limited in its ability to do so due to issues with the setup of the high-frequency environment. Further experiments must also be carried out to determine, with certainty, whether the observed energy increase in the low-frequency resonator is in fact a result of the theorized heat engine process. Finally, efforts to increase the quality factor of the sample must be made such that its value falls within the theorized range for autonomous heat engine operation.

References

[1] S. S. Gill *et al.*, "Quantum computing: Vision and challenges", in *Quantum Computing*. Elsevier, 2025, pp. 19–42, ISBN: 978-0-443-29096-1. DOI: 10.1016/B978-0-443-29096-1.00008-8.

[2] C. Degen, F. Reinhard, and P. Cappellaro, "Quantum sensing", *Rev. Mod. Phys.*, vol. 89, no. 3, p. 035 002, 2017, ISSN: 0034-6861, 1539-0756. DOI: 10.1103/RevModPhys.89.035002.

[3] N. Gisin, G. Ribordy, W. Tittel, and H. Zbinden, "Quantum cryptography", *Rev. Mod. Phys.*, vol. 74, no. 1, pp. 145–195, Mar. 2002, ISSN: 0034-6861, 1539-0756. DOI: 10.1103/RevModPhys.74.145.

[4] S. Djetel, S. Bégot, F. Lanzetta, E. Gavignet, and W. S. Bou Nader, "A Stirling Engine for Automotive Applications", in *Vehicle Power and Propulsion Conference*, Belfort, France, Dec. 2017.

[5] R. Tchinda and P. A. Ngouateu Wouagfack, "Optimization of absorption systems: case of the refrigerators and heat pumps", *Revue Africaine de Recherche en Informatique et Mathématiques Appliquées*, vol. Volume 30 - 2019 - MADEV health and energy (2017), Jun. 2019. DOI: 10.46298/arima.4360.

[6] G. Ripoll and J. José, *Quantum Information and Quantum Optics with Superconducting Circuits*, 1st ed. Cambridge University Press, Jul. 2022, ISBN: 978-1-316-77946-0. DOI: 10.1017/9781316779460.

[7] H. E. D. Scovil and E. O. Schulz-DuBois, "Three-level masers as heat engines", *Phys. Rev. Lett.*, vol. 2, pp. 262–263, 6 Mar. 1959. DOI: 10.1103/PhysRevLett.2.262.

[8] J. P. S. Peterson *et al.*, "Experimental characterization of a spin quantum heat engine", *Phys. Rev. Lett.*, vol. 123, no. 24, Dec. 2019, ISSN: 0031-9007, 1079-7114. DOI: 10.1103/PhysRevLett.123.240601.

[9] J. Rossnagel *et al.*, "A single-atom heat engine", *Science*, vol. 352, no. 6283, pp. 325–329, Apr. 2016, ISSN: 0036-8075, 1095-9203. DOI: 10.1126/science.aad6320.

[10] M. Rasola and M. Möttönen, "Autonomous quantum heat engine based on non-markovian dynamics of an optomechanical hamiltonian", *Sci. Rep.*, vol. 14, no. 1, Apr. 2024, ISSN: 2045-2322. DOI: 10.1038/s41598-024-59881-z.

[11] M. Rasola, V. Vadimov, T. Uusnäkki, and M. Möttönen, "Proposal for an autonomous quantum heat engine", Apr. 2025. DOI: 10.48550/arXiv.2502.08359.

[12] S. Probst, F. B. Song, P. A. Bushev, A. V. Ustinov, and M. Weides, "Efficient and robust analysis of complex scattering data under noise in microwave resonators", *Rev. Sci. Instrum.*, vol. 86, 2 Feb. 2015, ISSN: 0034-6748, 1089-7623. DOI: 10.1063/1.4907935.

[13] A. Blais, A. L. Grimsmo, S. M. Girvin, and A. Wallraff, "Circuit quantum electrodynamics", *Rev. Mod. Phys.*, vol. 93, 2 May 2021, ISSN: 0034-6861, 1539-0756. DOI: 10.1103/RevModPhys.93.025005.

[14] L. Frunzio, A. Wallraff, D. Schuster, J. Majer, and R. Schoelkopf, "Fabrication and characterization of superconducting circuit qed devices for quantum computation", *IEEE Transactions on Appiled Superconductivity*, vol. 15, pp. 860–863, 2 Jun. 2005, arXiv:cond-mat/0411708, ISSN: 1051-8223. DOI: 10.1109/TASC.2005.850084.

[15] C. Kiefer and E. Joos, "Decoherence: Concepts and examples", in *Quantum Future From Volta and Como to the Present and Beyond* (Lecture Notes in Physics), P. Blanchard and A. Jadczyk, Eds., Lecture Notes in Physics. Springer Berlin Heidelberg, 1999, vol. 517, pp. 105–128, ISBN: 978-3-540-65218-2. DOI: 10.1007/BFb0105342.

[16] A. A. Saki, M. Alam, and S. Ghosh, "Study of decoherence in quantum computers: A circuit-design perspective", Apr. 2019. DOI: 10.48550/arXiv.1904.04323.

[17] E. Joos and H. D. Zeh, "The emergence of classical properties through interaction with the environment", *Z. F. Z Phys. B. Con. Mat.*, vol. 59, no. 2, pp. 223–243, 2 Jun. 1985, ISSN: 0722-3277, 1434-6036. DOI: 10.1007/BF01725541.

[18] J. Bardeen, L. N. Cooper, and J. R. Schrieffer, "Theory of superconductivity", *Physical Review*, vol. 108, no. 5, pp. 1175–1204, Dec. 1957, ISSN: 0031-899X. DOI: 10.1103/PhysRev.108.1175.

[19] J. A. Flores-Livas, L. Boeri, A. Sanna, G. Profeta, R. Arita, and M. Eremets, "A perspective on conventional high-temperature superconductors at high pressure: Methods and materials", *Phys. Rep.*, vol. 856, pp. 1–78, Apr. 2020, ISSN: 03701573. DOI: 10.1016/j.physrep.2020.02.003.

[20] E. M. Purcell and D. Morin, *Electricity and Magnetism*, Third edition. Cambridge: Cambridge University Press, 2013, ISBN: 978-1-107-01402-2. DOI: 10.1017/CBO9781139012973.

[21] C. K. Alexander and M. N. O. Sadiku, *Fundamentals of electric circuits*, 3rd ed. Boston: McGraw-Hill Higher Education, 2007, ISBN: 978-0-07-297718-9.

[22] J. W. Nilsson and S. A. Riedel, *Electric circuits*, Eleventh edition. Hoboken, NJ: Pearson Education, Inc., 2019, ISBN: 978-0-13-474696-8.

[23] S. N. Makarov, R. Ludwig, and S. J. Bitar, *Practical electrical engineering*, Second edition. Cham: Springer, 2019, ISBN: 978-3-319-96691-5.

[24] A. Ciani, D. P. DiVincenzo, and B. M. Terhal, *Lecture Notes on Quantum Electrical Circuits*. TU Delft OPEN Books, 2025. DOI: 10.59490/tb.85.

[25] N. Zettili, *Quantum mechanics: concepts and applications*, 2. ed., repr. Chichester: Wiley, 2010, ISBN: 978-0-470-02678-6.

[26] P. Krantz, M. Kjaergaard, F. Yan, T. P. Orlando, S. Gustavsson, and W. D. Oliver, "A quantum engineer's guide to superconducting qubits", *App. Phys. Rev.*, vol. 6, 2 2019, ISSN: 1931-9401. DOI: 10.1063/1.5089550.

[27] R. E. Collin, *Foundations for microwave engineering* (IEEE Press series on electromagnetic wave theory), Second edition. New York Hoboken, New Jersey: IEEE Press, Wiley-Interscience, 2001, ISBN: 978-0-470-54466-2. DOI: 10.1109/9780470544662.

[28] D. Pozar, *Microwave Engineering*. Wiley, 2012, ISBN: 9781118213636.

[29] M. Göppl *et al.*, "Coplanar waveguide resonators for circuit quantum electrodynamics", *Jo. Appl. Phys.*, vol. 104, no. 11, p. 113 904, Dec. 2008, ISSN: 0021-8979, 1089-7550. DOI: 10.1063/1.3010859.

[30] M. Checchin, D. Frolov, A. Lunin, A. Grassellino, and A. Romanenko, "Measurement of the low-temperature loss tangent of high-resistivity silicon using a high- q superconducting resonator", *Phys. Rev. Appl.*, vol. 18, no. 3, p. 034 013, 2022, ISSN: 2331-7019. DOI: 10.1103/PhysRevApplied.18.034013.

[31] B. Antonio, *Physics and applications of the Josephson effect* (A Wiley-Interscience publication). New York: Wiley, 1982, ISBN: 978-3-527-60278-0. DOI: 10.1002/352760278X.

[32] J. M. Martinis and K. Osborne, "Superconducting qubits and the physics of josephson junctions", 2004. DOI: 10.48550/ARXIV.COND-MAT/0402415.

[33] B. D. Josephson, "The discovery of tunnelling supercurrents", *Rev. Mod. Phys.*, vol. 46, no. 2, pp. 251–254, Apr. 1974, ISSN: 0034-6861. DOI: 10.1103/RevModPhys.46.251.

[34] J. Clarke and A. I. Braginski, *The SQUID Handbook: Fundamentals and Technology of SQUIDs and SQUID Systems*, 1st ed. Wiley, May 2004, ISBN: 978-3-527-40229-8.

[35] J. Bardeen, L. N. Cooper, and J. R. Schrieffer, "Theory of superconductivity", *Phys. Rev.*, vol. 108, no. 5, pp. 1175–1204, Dec. 1957, ISSN: 0031-899X. DOI: 10.1103/PhysRev.108.1175.

[36] C. Timm, *Theory of Superconductivity*. TU Dresden: TU Dresden - Institute of Theoritical Physics, Apr. 2025.

[37] C. D. Tesche and J. Clarke, "Dc squid: Noise and optimization", *J. Low Temp. Phys.*, vol. 29, no. 3–4, pp. 301–331, Nov. 1977, ISSN: 0022-2291, 1573-7357. DOI: 10.1007/BF00655097.

[38] D. W. Phillip Thomas, "Electromagnetic compatibility for power electronics", in *Encyclopedia of Electrical and Electronic Power Engineering*. Elsevier, 2023, pp. 76–115, ISBN: 978-0-12-823211-8. DOI: 10.1016/B978-0-12-821204-2.00160-4.

[39] S. W. Sun, "Understanding the capacitive coupling with influence factors and applications", *J. Phys. Conf. Ser.*, vol. 1087, 2018, ISSN: 1742-6588, 1742-6596. DOI: 10.1088/1742-6596/1087/4/042011.

[40] M. Pierre, S. R. Sathyamoorthy, I.-M. Svensson, G. Johansson, and P. Delsing, "Resonant and off-resonant microwave signal manipulation in coupled superconducting resonators", *Phys. Rev. B*, vol. 99, no. 9, Mar. 2019, ISSN: 2469-9950, 2469-9969. DOI: 10.1103/PhysRevB.99.094518.

[41] M. Aspelmeyer, T. J. Kippenberg, and F. Marquardt, "Cavity optomechanics", *Rev. Mod. Phys.*, vol. 86, no. 4, pp. 1391–1452, Dec. 2014, ISSN: 0034-6861, 1539-0756. DOI: 10.1103/RevModPhys.86.1391.

[42] J. R. Johansson, G. Johansson, and F. Nori, "Optomechanical-like coupling between superconducting resonators", *Phys. Rev. A*, vol. 90, no. 5, Nov. 2014, ISSN: 1050-2947, 1094-1622. DOI: 10.1103/PhysRevA.90.053833.

[43] P. P. Potts, "Quantum thermodynamics", 2024. DOI: 10.48550/arXiv.2406.19206.

[44] R. Weber, S. F. Huelga, and M. B. Plenio, "The thermodynamic costs of pure dephasing in quantum heat engines: Quasistatic efficiency at finite power", 2023. DOI: 10.48550/ARXIV.2312.05375.

[45] K. Ito *et al.*, "Universal relations and bounds for fluctuations in quasistatic small heat engines", *Commun. Phys.*, vol. 8, no. 1, p. 60, Feb. 2025, ISSN: 2399-3650. DOI: 10.1038/s42005-025-01961-1.

[46] S. Deffner and S. Campbell, *Quantum Thermodynamics: an Introduction to the Thermodynamics of Quantum Information* (IOP Concise Physics). San Rafael: Morgan Claypool Publishers, 2019, ISBN: 978-1-64327-658-8.

[47] S. R. Systems, *Vector signal generator - sg390 series*, 2025. [Online]. Available: https://www.thinksrs.com/products/sg390.html.

[48] F. Marki and C. Marki, *Mixer basics primer*, May 2023. [Online]. Available: https://markimicrowave.com/technical-resources/white-papers/mixer-basics-primer/.

[49] D. Jorgesen, *Iq/ir/ssb mixer primer*, May 2020. [Online]. Available: https://markimicrowave.com/technical-resources/white-papers/iq-ir-ssb-mixer-primer/.

[50] M. Rasola *et al.*, "Low-characteristic-impedance superconducting tadpole resonators in the sub-gigahertz regime", en, *Physical Review Research*, vol. 6, no. 4, p. 043 297, Dec. 2024, ISSN: 2643-1564. DOI: 10.1103/PhysRevResearch.6.043297.